The Thesis committee for Preeti Kumari

Certifies that this is the approved version of the following thesis

IEEE 802.11ad V2V-Radar: A Joint Vehicle-to-Vehicle Communication and Automotive Radar System

APPROVED BY

SUPERVISING COMMITTEE:

Robert W. Heath, Jr., Supervisor

Joydeep Ghosh

IEEE 802.11ad V2V-Radar: A Joint Vehicle-to-Vehicle Communication and Automotive Radar System

by

Preeti Kumari, B.Tech.

THESIS

Presented to the Faculty of the Graduate School of

The University of Texas at Austin

in Partial Fulfillment

of the Requirements

for the Degree of

MASTER OF SCIENCE IN ENGINEERING

THE UNIVERSITY OF TEXAS AT AUSTIN

May 2016

Acknowledgments

I would like to express my deepest gratitude to my supervisor, Prof. Robert W. Heath, Jr. for his valuable insights, constant support and encouragement during the course of this research.

I would especially like to thank my committee member Prof. Joydeep Ghosh. Without his priceless advice and support, this work would not have been possible.

I gratefully acknowledge the support of Prof. Nuria G. Prelcic, Universidade de Vigo and Dr. Junil Choi, UT Austin for their help and support.

I would also like to thank my friends and colleagues at UT Austin, particularly Ahmed Alkhateeb, Abhishek Sankaraman, Andrew Thornburg, Anum Ali, Dr. Duy H. N. Nguyen, Hardik Jain, Jianhua Mo, Kiran Venugopal, Michael LeBeane, Dr. Mohammed E. Eltayeb, Sara Mourad, Talha Ahmed Khan, and Vutha Va for helpful discussions and for providing enough laughs, support and entertainment in my life.

Special thanks to my family members to whom I will ever be indebted.

IEEE 802.11ad V2V-Radar: A Joint Vehicle-to-Vehicle Communication and Automotive Radar System

by

Preeti Kumari, M.S.E.
The University of Texas at Austin, 2016

Supervisor: Robert W. Heath, Jr.

Proprietary millimeter wave (mmWave) radar technologies are widely used in luxury cars to enable active safety functions such as cruise control and collision avoidance. Vehicle-to-vehicle (V2V) communication using the dedicated short range communication (DSRC) technology permits basic low-latency safety applications such as forward collision detection in the 5.9 GHz band. The DSRC technology supports only low data rates, which is not sufficient to handle the gigabytes that can be generated in the next generation vehicles. This challenge can, however, be overcome by using mmWave V2V communication technology that has not been adopted yet by the automotive industry. In this thesis, we propose an IEEE 802.11ad V2V-radar system that leverages the waveform and the typical receiver algorithms of a mmWave consumer WLAN standard to enable a joint framework of vehicular communication and radar technologies at 60 GHz. It will lead to efficient spectrum usage, enhanced performance and increased penetration in the vehicles with

minimal size and cost of the hardware. Our theoretical analyses and numerical simulations show promising results; Gbps data rate is achieved simultaneously with cm-level range accuracy, cm/s-level velocity accuracy and high probability of detection at a significantly low false alarm rate.

Table of Contents

List of Figures

Chapter 1

Introduction

Vehicular communication and radar sensing are the two primary means of using radio frequency (RF) signals to improve traffic safety and efficiency. Automotive radars provide a high-resolution sensing map for continuous automatic vehicle detection using proprietary waveforms at the mmWave band [1,2]. Long-range radar (LRR) operates in the $76-77$ GHz mmWave band and is used for adaptive cruise control. Short-range radar (SRR) operates in the newer $77-81$ GHz mmWave band and is used for parking aid and pre-crash applications. Automotive radars are expensive and are already deployed in a large number of luxury vehicles [3].

V2V communication allows vehicles to achieve real-time cooperative detection and ranging for applications such as forward collision warning and cooperative adaptive cruise control [4]. DSRC is a low-latency vehicular communication protocol that operates using a WLAN-based physical layer in the 5.9 GHz microwave band and supports data rates in the range of $3-6$ Mbps in practice [5]. The low data rate may restrict the next generation of connected vehicles, which would require exchanging raw sensor data between vehicles at Gbps data rates [6]. A solution to realize Gbps data rates is to exploit the large

bandwidths available in the mmWave spectrum. This can be achieved through a modification of the IEEE 802.11ad standard, the forthcoming mmWave 5G cellular standard (either by directly using device-to-device mode or by using future employed cellular infrastructure), or the development of a dedicated mmWave vehicular communication technology [6].

Although both radar and communication technologies have applications to driver-assist and autonomous driving, they have their own domain specific challenges and limitations. A joint communication and radar system that shares the same spectrum and hardware will, however, lead to an increase in the penetration rate of communication and radar in vehicles. It will also reduce size and cost of the hardware with efficient spectrum usage and enhanced security. Additionally, using both technologies simultaneously in an integrated unit will allow vehicles to reap the advantage of each technology (e.g., radar for non-communicating traffic and V2V for distances beyond the LOS constraints of radar) and enhance their performance by sharing information with each other.

In the past half-decade a number of approaches for joint radar and communication which exploit existing radar and communication waveforms have been considered (see, e.g., [7] and the references therein). The approaches can be mainly classified into a joint system, where a single-carrier or a multi-carrier waveform is used for both communication and radar simultaneously, and a time-domain duplex system, where radar and communication will operate in different time cycles.

In single-carrier systems, direct-sequence spread spectrum (DSSS) [8] and chirp spread spectrum (CSS) [9] have been widely used for fusing radar and communication functions. In DSSS based joint system [8], the transmit waveform cannot simultaneously achieve the ideal cross-correlation properties for communication and ideal auto-correlation properties for radar functions. This limits the radar ranging capability with Doppler shift sensitivity and reduces the communication data rate. Additionally, the system implementation suffers from high complexity of the correlation-based Doppler estimator and low spectral efficiency. In [9], both communication and radar waveforms are linear frequency modulated (LFM) signals in the same frequency range and they are implemented by leveraging quasi-orthogonality of the up-chirp (for communication functionality) and the down-chirp (for radar functionality). The experimental results in [9] illustrated that simultaneous operation may not be optimal due to the mutual interference that might exist between communication and radar signals.

In multi-carrier schemes, OFDM waveforms are popular for implementing joint radar and communication systems [8, 10, 11]. In [10], radar parameters are estimated using classic correlation-based (matched filter) processing approach on OFDM waveforms, whereas in [8], the radar parameter estimation algorithms use only Fourier transforms. The Fourier based algorithms allow faster processing and lesser sidelobe levels compared to [10]. The sidelobe levels in [8], however, is still not ideal for radar ranging and they degrade processing gain and ranging resolution. In [11], the IEEE 802.11p V2V com-

munication standard is analyzed for automotive radars similar to [8] and they do not achieve cm-level range and cm/s-level velocity accuracy that is desirable in automotive radars [12]. OFDM-based integrated systems in [8, 10, 11], also suffer from high peak-to-average power ratio (PAPR) of OFDM signals, unlike traditional radars that have PAPR of 0 dB.

In a time-domain duplex paradigm, existing radar (esp. FMCW radar) and communication waveform techniques are exploited [7, 13, 14]. This approach provides high spectral efficiency, is low cost and easy to implement, and introduces less mutual interference between radar and communication than the joint waveform [7]. The main limitation of this approach is that it suffers from a high peak-to-sidelobe ratio for radar detection and it has a poor efficiency for data transmission.

In this thesis, we develop an IEEE 802.11ad V2V-radar system that enables both V2V communication and LRR technologies to exploit the same mmWave spectrum and to leverage shared hardware based on the mmWave consumer WLAN standard. This approach motivates a common standard for automotive radar and vehicular communications at the mmWave band. Indeed, the most prevalent V2V standard, DSRC, is based on IEEE 802.11p, which is an evolution of a WLAN standard known as IEEE 802.11a. IEEE 802.11p, however, operates at 5.9 GHz and not at the mmWave frequency bands. Using a mmWave standard will provide access to large bandwidth, which will lead to significant advantages in terms of higher data rates for communication and better accuracy/resolution for radar operation than IEEE

802.11p. This will also allow to simultaneously achieve ultra-low latency and high range of operation for automotive safety applications with minimal hardware size and cost. The contributions of this thesis are summarized as follows:

- A doubly selective mmWave system model is proposed that includes radar-centric (target and clutter model in a coherent processing interval) channel description in the WLAN-based transmitter and receiver signal model.

- Multi-frame pulse-Doppler based radar algorithms are developed that exploit the special structure of IEEE 802.11ad preamble and standard WLAN techniques per frame to enhance the performance of the IEEE-802.11ad V2V-radar system.

- Numerical simulations are provided to characterize the performance of the IEEE 802.11ad V2V-radar system. The results indicate that the proposed framework can meet the desired LRR range accuracy requirement of 0.1 m and velocity accuracy requirement of 0.1 m/s with very high probability of detection at a significantly low false alarm rate [12]. It also shows that it is possible to simultaneously achieve cm-level range and cm/s-level velocity estimation accuracy with Gbps communication data rate in a coherent processing interval (CPI) of 0.06 ms.

- Performance evaluation using Cramer Rao lower bound (CRLB) is provided to give additional insight to the numerical results. The trade-off

between between LRR and V2V communication performance is also evaluated.

Our previous work in [15] is the first to propose the idea of using IEEE 802.11ad for a joint V2V and automotive radar system. There were some limitations in [15]: 1) the system model was developed only for a single frame and it did not include clutter model and false alarm rate detection performance metric; 2) the Doppler shift estimation was not accurate enough at low and medium signal-to-noise ratio (SNR); and 3) it did not provide a theoretical insight to the performance of the IEEE 802.11ad-based V2V. This thesis overcomes these limitations and provides a further in-depth analysis and simulation of the proposed IEEE 802.11ad V2V-radar system.

The rest of the thesis is organized as follows. A summary of the preamble sequences for a single carrier physical layer (SCPHY) frame of IEEE 802.11ad is included in chapter II. In chapter III, an integrated system model of LRR and V2V is developed. chapter IV proposes different single- and multiple- frame processing techniques and analyzes their theoretical performance for radar parameter estimation. Numerical results and performance evaluations are described in chapter V, while the conclusion follows in chapter VI.

Notation: We use the following notation throughout the thesis: vectors are denoted by boldface lower case letters $\mathbf{a}$, matrices by boldface capital letters $\mathbf{A}$, and scalar values by a, A. The n^{th} component of vector $\mathbf{a}$ is written

as $a[n]$ and the $(\ell, m)^{\text{th}}$ element of matrix $\mathbf{A}$ is denoted by $A[\ell, m]$. We use the notation $||\mathbf{c}||$ for the ℓ_2 norm of $\mathbf{c}$ and $\mathbf{A} \otimes \mathbf{B}$ for the Kronecker product of $\mathbf{A}$ and $\mathbf{B}$. $||\mathbf{A}||_{\text{F}}$ is the Frobenius norm, $\mathbf{A}^*$ is the conjugate transpose, $\mathbf{A}^{\text{T}}$ is the transpose, and $\mathbf{A}^{\text{c}}$ is the conjugate of matrix $\mathbf{A}$. We use the notation $\mathcal{CN}(\mu, \sigma^2)$ to denote a complex circularly symmetric Gaussian random variable with mean μ and variance σ^2. The expression $\Re\{a\}$ is used to denote the real part of a and the notation $h(t) * x(t)$ is used to denote the convolution between the two signals $h(t)$ and $x(t)$.

Chapter 2

Overview of IEEE 802.11ad Standard

In this thesis, we leverage the special structure of the preamble of the SCPHY frames for demonstrating the use of IEEE 802.11ad for automotive radar applications. We, therefore, review key features of the IEEE 802.11ad frame in this chapter, focusing on the preamble structure of SCPHY frame. The preamble in SC PHY frame is similar to other physical layer (PHY) frames of IEEE 802.11ad, i.e. OFDM PHY frame and control PHY frame, and therefore, the findings using SCPHY modulation can be easily extended to other PHY modulations. Additionally, it does not suffer from PAPR issue as OFDM PHY frame and is more probable to be frequency used than control PHY frame.

An IEEE 802.11ad SCPHY frame is composed of a short training field (STF), a channel estimation field (CEF), a header, data blocks (BLKs), and optional beam training fields, as shown in Fig. 2.1. The preamble of the IEEE 802.11ad frame is composed of the STF and the CEF and is generated from a pair of 128 chip Golay complementary sequences (GCSs), termed $\mathbf{Ga}_{128}$ and $\mathbf{Gb}_{128}$ [16], as shown in Fig. 2.2 and Fig. 2.3. The GCSs $\mathbf{Ga}_{128}$ and $\mathbf{Gb}_{128}$ are defined in Section 21.11 of [17].

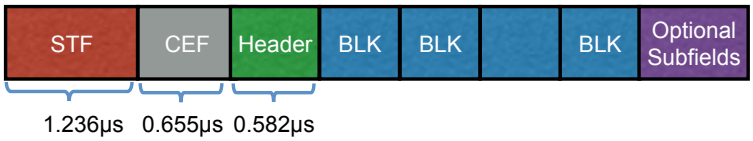

Figure 2.1: Frame structure of IEEE 802.11ad SCPHY.

Figure 2.2: Extracted short training field for a SCPHY frame.

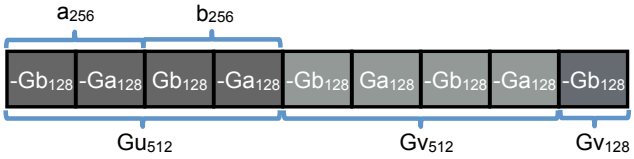

Figure 2.3: Extracted channel estimation field for a SCPHY frame.

2.1 Frame Structure

The STF is used in communication for frame synchronization and frequency offset estimation. It is composed of sixteen repeated $\mathbf{Ga}_{128}$ followed by the binary complement of $\mathbf{Ga}_{128}$, i.e., $-\mathbf{Ga}_{128}$. The boundary between the STF and the CEF is provided by $-\mathbf{Ga}_{128}$, which can also be expressed in terms of 32 sample GCP, termed $\mathbf{Ga}_{32}$ and $\mathbf{Gb}_{32}$, as

$$-\mathbf{Ga}_{128} = \left[-\mathbf{Gb}_{32} \quad -\mathbf{Ga}_{32} \quad \mathbf{Gb}_{32} \quad -\mathbf{Ga}_{32}\right]. \tag{2.1}$$

The CEF is used to estimate the communication channel parameters and to indicate the modulation of the packet (e.g., SCPHY or OFDM physical layer). It consists of a 512 sample GCP, denoted by $[\mathbf{Gu}_{512} \ \mathbf{Gv}_{512}]$ and is

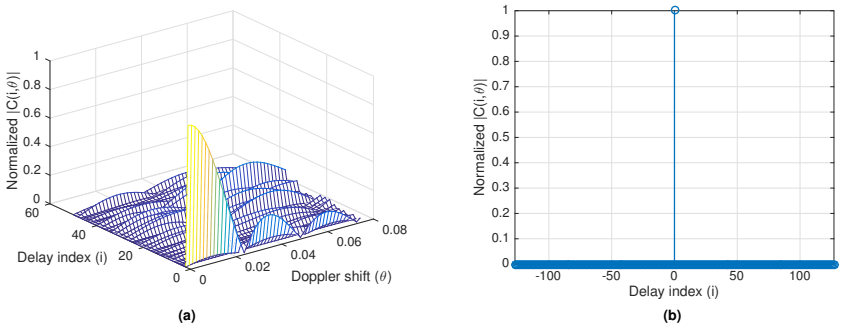

Figure 2.4: (a) The composite ambiguity function of the 128 sample GCP, which are used in the preamble of IEEE 802.11ad. (b) The zero-Doppler cut of the composite ambiguity function of (a).

followed by $\mathbf{Gv}_{128}$, which is a binary complement of $\mathbf{Gb}_{128}$. The GCSs $\mathbf{Gu}_{512}$ and $\mathbf{Gv}_{512}$ are defined as

$$\mathbf{Gu}_{512} = \left[-\mathbf{Gb}_{128} \quad -\mathbf{Ga}_{128} \quad \mathbf{Gb}_{128} \quad -\mathbf{Ga}_{128}\right], \tag{2.2}$$

$$\mathbf{Gv}_{512} = \left[-\mathbf{Gb}_{128} \quad \mathbf{Ga}_{128} \quad -\mathbf{Gb}_{128} \quad -\mathbf{Ga}_{128}\right]. \tag{2.3}$$

As shown in Fig. 3, the structure of the CEF is based on the various combinations of $\mathbf{Ga}_{128}$ and $\mathbf{Gb}_{128}$, which can be leveraged to achieve the ideal ambiguity function for automotive radars at zero-Doppler shift.

2.2 Composite Ambiguity Function

The ambiguity function of a training sequence $\mathbf{p} = \{p[n]\}$ of length P is defined as [18]

$$A(\mathbf{p}, i, \theta) = \sum_{n=1}^{P-i} p[n]p[n+i]e^{jn\theta}, \tag{2.4}$$

where θ represents the relative Doppler shift (in radians) during a chip interval (T_{s}), and the discrete index i denotes a delay of iT_{s} seconds. The composite ambiguity function, $\mathrm{CAF}(i,\theta)$, of P sample GCSs $\mathbf{u}_{\mathrm{P}} = \{u_{\mathrm{P}}[n]\}$ and $\mathbf{v}_{\mathrm{P}} = \{v_{\mathrm{P}}[n]\}$ is defined as [19]

$$\mathrm{CAF}(i,\theta) = A(\mathbf{u}_{\mathrm{P}}, i, \theta) + e^{jP\theta} A(\mathbf{v}_{\mathrm{P}}, i, \theta), \tag{2.5}$$

where $A(\mathbf{u}_{\mathrm{P}}, i, \theta)$ and $A(\mathbf{v}_{\mathrm{P}}, i, \theta)$ are the ambiguity functions for $\{u_{\mathrm{P}}[n]\}$ and $\{v_{\mathrm{P}}[n]\}$, respectively. Here, the delay is considered in discrete-time because we are calculating the ambiguity function of a discrete-time sequence. Ambiguity function of the discrete-time signal after convolution with a pulse shaping filter will be a function of continuous time delay and can be similarly obtained based on the choice of the pulse shaping filter. The value of the ambiguity function for the discrete sequence with any pulse shaping filter at delay of iT_{s} will, however, remain same as the value of the ambiguity function for the discrete sequence at delay index i.

The composite ambiguity function of the 128 sample GCP shown in Fig. 2.4 motivates its suitability as a radar waveform [20]. The zero-Doppler cut of the composite ambiguity function indicates that the GCP has a perfect auto-correlation with no sidelobe along the zero Doppler axis. This characteristic makes it ideal for target detection in radar applications, which does not exist in FMCW signals typically used in LRR [21, 22]. This figure also shows that the GCP is less tolerant to large Doppler shifts. These sequences, however, seem to be appropriate for LRR due to the low Doppler shift inherent

in the vehicular environment.

Chapter 3

System Model

In this chapter, we formulate the signal model for the joint automotive radar and V2V communication system based on the IEEE 802.11ad standard. First, we discuss the vehicular scenario of interest and the transmit signal model. Then, we develop the channel model and the analog beamforming vectors to derive the received signal model for both radar and communication systems.

3.1 Vehicular Scenario

We consider a use case for joint vehicular communication and radar, where a source vehicle sends a waveform to a target vehicle using the IEEE 802.11ad-based V2V communication service. The IEEE 802.11ad waveform may get reflected back from the target vehicle and the other surrounding scatters (e.g., trees, road, and the other remote vehicles) as shown in Fig. 3.1. Then, the source vehicle receives these reflected echoes from the scatters in a full-duplex configuration and derives information about the target vehicle [23]. We assume a multiple antenna joint communication-radar system with N_{T} co-located transmit (TX) antennas and N_{R} co-located receive (RX) antennas

mounted on the source and the target vehicles. This assumption will allow us to evaluate the trade-off between the radar performance at the source vehicle with the communication performance at the target vehicle. The TX and the RX antenna arrays on the source vehicle are closely separated such that both arrays will see the same location parameters (e.g., azimuth/elevation angle and range) of a scatter and the separation provides isolation between the transmitter and the receiver to reduce the full-duplex effect. We also consider that the TX/RX beams of the source vehicle are pointed towards the target vehicle without blockage and that the 3-dB beamwidth of the TX and RX beams are narrow during mmWave V2V communication [24–26]. Although very narrow beamwidth will lead to less clutter interference and long range of operation, it can yield poor performance with vehicle mobility and blockage [26–28]. Hence, we assume that the TX/RX beams are narrow enough to meet the link budget requirement of V2V communication but are wide enough to illuminate all the scattering centers of a far target vehicle within their resolution [12, 26]. Therefore, we represent the target vehicle as a single point target, as in [29, 30].

3.2 Transmit Signal

Let $\Re\left\{x(t)e^{j2\pi f_c t}\right\}$ denote the passband continuous-time IEEE 802.11ad waveform with carrier frequency f_c at time t. The complex baseband continuous-

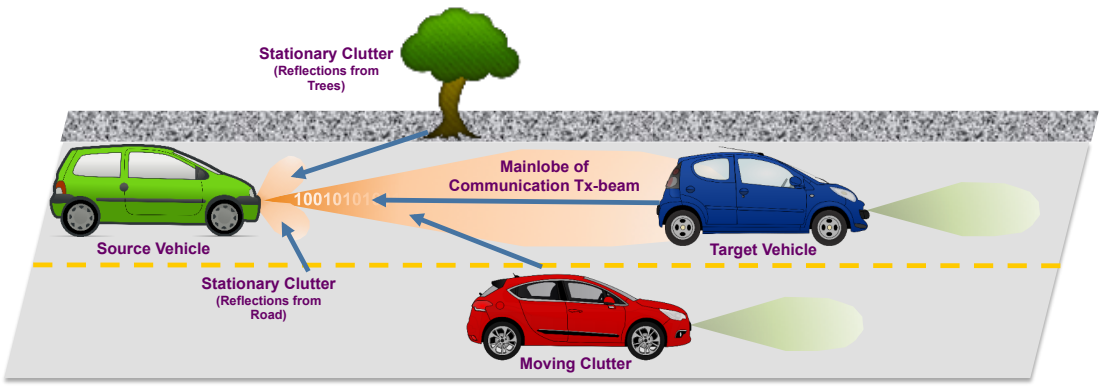

Figure 3.1: Illustration of a traffic scenario for joint automotive radar and vehicular communication systems using IEEE 802.11ad.

time representation of the waveform is

$$x(t) = \sqrt{\mathcal{E}_{\mathrm{s}}} \sum_{n=-\infty}^{\infty} s[n] g_{\mathrm{T}}(t - nT_{\mathrm{s}}), \tag{3.1}$$

where $\mathcal{E}_{\mathrm{s}}$ is the signal energy per symbol at the transmitter, $g_{\mathrm{T}}(t)$ is the unit energy transmit pulse-shaping filter, i.e., $\int_{-\infty}^{\infty} |g_{\mathrm{T}}(t)|^2 dt = 1$, T_{s} is the chip duration and $\{s[n]\}$ is the transmitted symbol sequence corresponding to a single-carrier waveform of IEEE 802.11ad. The chip duration is related to the signaling bandwidth (W) as $T_{\mathrm{s}} \approx 1/W$. The IEEE 802.11ad specification defines the receive filter for error vector magnitude (EVM) measurement as a root-raised cosine (RRC) filter with a roll-off factor of 0.25. Therefore, in numerical simulations, we have assumed a unit energy root raised cosine waveform for the transmit pulse shaping filters $g_{\mathrm{T}}(t)$ and the receive pulse shaping filter $g_{\mathrm{R}}(t)$.

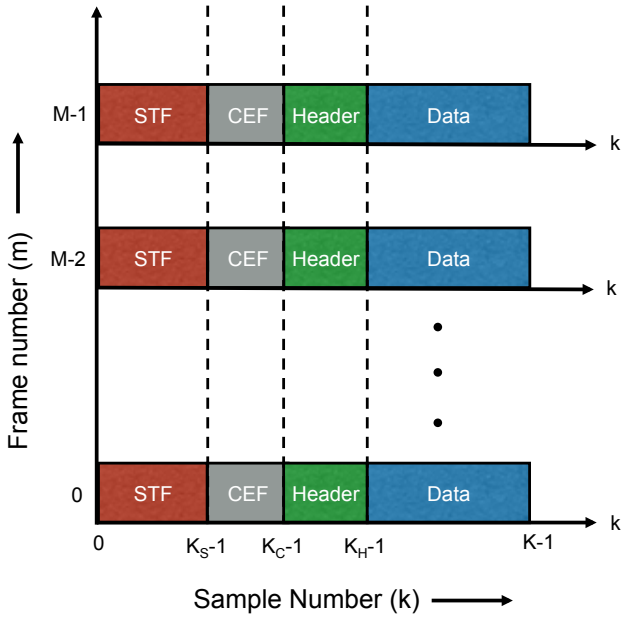

Figure 3.2: Illustration of a coherent pulse interval (CPI) which consists of M frames, each of K samples. The end positions of the STF, the CEF and the header are K_{S}-1, K_{C}-1, and K_{H}-1, respectively.

3.3 Channel Model

We now consider a single coherent processing interval (CPI) of $T = MKT_{\mathrm{s}}$ duration which is comprised of M frames, each of K samples, as shown in Fig. 3.2. We can conceptually represent the data of a CPI by a four dimensional (4-D) data cube with the following axes:

1. Sample number within a frame (k): This dimension represents the sample index (k) within a frame sampled at the highest rate W of the system. This axis in pulse Doppler radar terminology is known as *fast-time axis* and is used to estimate the delay of the target vehicle using a single

pulse [31].

2. Frame number (M): A vector $\mathbf{p} \in \mathbb{C}^{M\times 1}$ in this dimension contains samples from M consecutive frames corresponding to the same delay bin, i.e., k. This axis in pulse Doppler radar terminology is known as *slow-time axis* and is used to estimate the Doppler shift in a single CPI [31].

3. TX/RX channel axes: These axes represent the same frame transmitted across N_{T} TX array elements and received across N_{R} RX array elements, respectively. Analysis of the samples across this dimension is used to examine spatial frequency content of each received frame. The resolution of TX angle of departure (AoD) is governed by $\Delta\psi_{\mathrm{T}} = 1/N_{\mathrm{T}}$ and of RX angle of arrival (AoA) is governed by $\Delta\psi_{\mathrm{R}} = 1/N_{\mathrm{R}}$.

The mmWave sensing channel during a CPI is comprised of a few scattering centers [32], which represent reflections from the target vehicle and the other surrounding objects. The vehicular channel has a key characteristic of temporal variability and inherent non-stationarity [33]. The description of channel in azimuth and elevation directions is also critical for mmWave arrays used in vehicular radar and communication applications [25,34]. Therefore, we model the mmWave channel for a single CPI as a doubly selective (time- and frequency-selective) mmWave channel with a few N_{p} dominant paths and 2-D TX and RX steering vectors. Each p^{th} path is described by five physical parameters: its azimuth and elevation AoA pair $(\phi_{\mathrm{R},p}, \theta_{\mathrm{R},p})$, AoD pair $(\phi_{\mathrm{T},p}, \theta_{\mathrm{T},p})$, delay τ_p, complex gain α_p and Doppler shift ν_p. The steering vectors $\mathbf{b}(\phi, \theta)$

for mmWave arrays in azimuth angle ϕ and elevation angle θ can be described as a Kronecker product of array steering vectors in the azimuth and elevation directions, i.e.,

$$\mathbf{b}(\phi,\theta) = \mathbf{b}_{\text{az}}(\phi) \otimes \mathbf{b}_{\text{el}}(\theta). \tag{3.2}$$

In particular, for an N_{az} element uniform linear array (ULA) in the azimuth direction the steering vector is given by

$$\mathbf{b}_{\text{az}}(\phi) = \frac{1}{\sqrt{N_{\text{az}}}}[1, e^{-j2\pi\frac{q}{\lambda}\sin(\phi)}, e^{-j4\pi\frac{q}{\lambda}\sin(\phi)}, \cdots, e^{-j2\pi\frac{q}{\lambda}(N_{\text{az}}-1)\sin(\phi)}]^{\text{T}}, \tag{3.3}$$

where q denotes the antenna spacing [35] and ϕ for the 0^{th} path corresponding to the two-way radar channel with AoD azimuth angle ϕ_0 and AoA azimuth angle $\phi_{\text{R,rad},0}$ and the one-way communication channel with AoD azimuth angle ϕ_0 and AoA azimuth angle $\phi_{\text{R,com},0}$ is defined as in Fig. 3.3. We can also from Fig. 3.3 that $\phi_{\text{R,com},0} = \phi_0 = \phi_{\text{R,rad},0} - 180^o$ for ρ_0 much greater than the spacing between the TX and the RX array. The array steering vector $\mathbf{b}_{\text{el}}(\theta)$ in the elevation direction can be similarly described for an N_{el}-element ULA.

The multiple-antenna communication/radar channel between the transmitter and the receiver, $\mathbf{H}_{\text{p}}(t,f) \in \mathbb{C}^{N_{\text{R}}\times N_{\text{T}}}$, can be described in terms of multi-path model as [36, 37]

$$\mathbf{H}_{\text{p}}(t,f) = \sqrt{\frac{1}{N_{\text{p}}}} \sum_{p=0}^{N_{\text{p}}-1} \alpha_p e^{j2\pi\nu_p t} e^{-j2\pi\tau_p f} e^{j2\pi(\nu_p - f_{\text{c}})\tau_p} \mathbf{b}_{\text{R}}(\phi_{\text{R},p},\theta_{\text{R},p}) \mathbf{b}_{\text{T}}^{*}(\phi_{\text{T},p},\theta_{\text{T},p}), \tag{3.4}$$

where $\mathbb{E}\left[||\mathbf{H}_{\text{p}}(t,f)||_{\text{F}}^2\right] = 1$. The terms $\mathbf{b}_{\text{T}}(\phi_{\text{T},p},\theta_{\text{T},p}) = \mathbf{b}_{\text{T,az}}(\phi_{\text{T},p}) \otimes \mathbf{b}_{\text{T,el}}(\theta_{\text{T},p})$ and $\mathbf{b}_{\text{R}}(\phi_{\text{R},p},\theta_{\text{R},p}) = \mathbf{b}_{\text{R,az}}(\phi_{\text{R},p}) \otimes \mathbf{b}_{\text{R,el}}(\theta_{\text{R},p})$ denote the transmit and receive steering vectors.

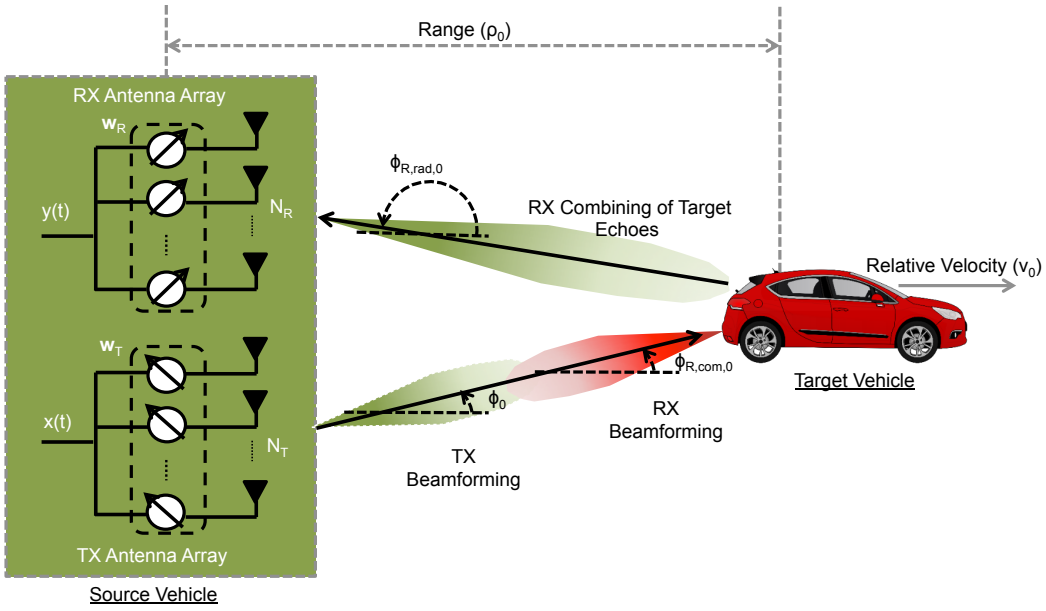

Figure 3.3: After the IEEE 802.11ad beam alignment procedure described in Chapter 3.4, the TX and RX beams are pointed towards the target vehicle whose scattering centers falls within the single resolution cell. As the distance between the source vehicle and the target vehicle increases, the $\phi_{\mathrm{R,rad},0}$ at the source vehicle converges to $180^o + \phi_0$.

Without loss of generality, we assume the LOS two-way path from the source vehicle to the single point target representing the target vehicle (which is also the user of V2V communication link established by the source vehicle) is represented by the 0^{th} path. The point target is assumed to be at an arbitrary range $\rho_0(t)$ with a two-way round-trip propagation delay of $\tau_0(t)$ from the reference point on the TX array of the source vehicle to its reference point on the RX array. In vehicular applications, a target vehicle is a slowly moving target compared to the speed of light c and hence, a quasi-stationary assumption can be made [38]. This assumption implies that the

range change during the short path of any particular point in the waveform from the transmitter to the receiver is negligible. With this assumption, the two-way round-trip propagation delay at time t is

$$\tau_0(t) = \frac{2\rho_0(t)}{c}. \tag{3.5}$$

We assume that the target velocity relative with respect to the source vehicle is small enough, i.e., $v \ll c/2TW$ to allow for constant location, that is, constant ρ_0, τ_0 (we drop t from $\rho_0(t)$ and $\tau_0(t)$ because they are assumed to be constant for the time of interest), and azimuth/elevation AoD pair (ϕ_0, θ_0) and AoA pair $(180^0 + \phi_0, 180^0 + \theta_0)$ during the CPI [39]. We also assume that the target vehicle has an arbitrary relative radial velocity of v with respect to the source vehicle. It remains constant within the CPI because of small acceleration (ε_0), i.e., $\varepsilon_0 \ll c/2f_cT^2$ [39]. The Doppler shift, therefore, can be represented by

$$\nu_0 = 2\frac{v}{\lambda}, \tag{3.6}$$

where λ is the carrier wavelength. In the channel model, we only consider far targets whose ρ_0 is large compared to the distance change during the CPI, i.e., $\rho_0 \gg v/T$. Hence, we assume constant a complex gain α_0 for the target vehicle [39, 40].

The time-varying frequency response matrix $\mathbf{H}_{\mathrm{p}}(t, f)$ is non-linearly dependent on the physical parameters, making it difficult to analyze and estimate the parameters. Additionally, the low-complexity typical WLAN receiver algorithms described in chapter-4, estimates delay with resolution $\Delta\tau = 1/W$,

Doppler shift with resolution $\Delta\nu = 1/T_{\text{int}}$ with integration time $T_{\text{int}} = K_{\text{S}}T_{\text{s}}$. Therefore, low-complexity radar receiver algorithms proposed in chapter-4 that are based on typical WLAN RX algorithms using single frame have same resolution as the typical WLAN RX algorithms and low-complexity multi-frame Doppler estimation has a resolution of $\Delta\nu = 1/T_{\text{int}}$ with $T_{\text{int}} = T$. The codebook for beamforming is not explicitly described in the IEEE 802.11ad standard and it limits the resolution of AoD and AoA. We mimic these effects by assuming the codebook to be DFT vectors with AoD resolution of $\Delta\phi_{\text{T}} = 1/N_{\text{T}}$, and AoA resolution of $\Delta\phi_{\text{R}} = 1/N_{\text{R}}$ and by using the virtual channel representation to develop an approximation of $\mathbf{H}_{\text{p}}(t, f)$ via uniform sampling in delay, Doppler and angular dimension commensurate with resolution in their respective dimension [41–43]. Design of high resolution radar parameter estimation using low-complexity advanced receiver algorithms in a joint radar and communication framework can be explored in future work.

To develop the virtual channel model, we further develop the system model using a one-dimensional N_{T} element TX ULA and N_{R} element RX ULA, i.e., we assume $\mathbf{b}_{\text{T,el}}(\theta_{\text{T},p}) = 1$, $\mathbf{b}_{\text{R,el}}(\theta_{\text{R},p}) = 1$, and $\mathbf{b}_{\text{T,az}}(\phi_{\text{T},})$ and $\mathbf{b}_{\text{R,az}}(\phi_{\text{R},p})$. The constant phase shift $e^{j2\pi(\nu_p - f_{\text{c}})\tau_p}$ in (3.4) does not effect the magnitude or Doppler shift of the p^{th} path and can be ignored [44]. Therefore, the time-varying frequency response matrix, $\mathbf{H}_{\text{p}}(t, f)$, in (3.4) can be simplified for ULA TX/RX arrays as

$$\mathbf{H}_{\text{p}}(t, f) = \sqrt{\frac{1}{N_{\text{p}}}} \sum_{p=0}^{N_{\text{p}}-1} \alpha_p e^{j2\pi\nu_p t} e^{-j2\pi\tau_p f} \mathbf{a}_{\text{R}}(\phi_{\text{R},p}) \mathbf{a}_{\text{T}}^{*}(\phi_{\text{T},p}), \tag{3.7}$$

where $\mathbf{a}_{\mathrm{R}}(\phi_{\mathrm{R},p}) = \mathbf{b}_{\mathrm{R,az}}(\phi_{\mathrm{R},p})$ and $\mathbf{a}_{\mathrm{T}}(\phi_{\mathrm{T},p}) = \mathbf{b}_{\mathrm{T,az}}(\phi_{\mathrm{T},p})$. Then the virtual representation of (3.7) is given by

$$\mathbf{H}_{\mathrm{p}}(t,f) \approx \sum_{\xi=1}^{N_{\mathrm{R}}} \sum_{\eta=1}^{N_{\mathrm{T}}} \sum_{\ell=0}^{L-1} \sum_{d=-D}^{D} H_{\mathrm{v}}(\xi,\eta,\ell,d) \mathbf{a}_{\mathrm{R,v}}\left(\frac{\xi}{N_{\mathrm{R}}}\right) \mathbf{a}_{\mathrm{T,v}}^{*}\left(\frac{\eta}{N_{\mathrm{T}}}\right) e^{-j2\pi\frac{\ell}{W}f} e^{j2\pi\frac{d}{T}t} \tag{3.8}$$

where,

$$\mathbf{a}_{\mathrm{R,v}}\left(\frac{\xi}{N_{\mathrm{R}}}\right) = \mathbf{a}_{\mathrm{R}}\left(\arcsin\left(\frac{\lambda}{d}\frac{\xi}{N_{\mathrm{R}}}\right)\right), \tag{3.9}$$

$$\mathbf{a}_{\mathrm{T,v}}\left(\frac{\eta}{N_{\mathrm{R}}}\right) = \mathbf{a}_{\mathrm{T}}\left(\arcsin\left(\frac{\lambda}{d}\frac{\eta}{N_{\mathrm{T}}}\right)\right), \tag{3.10}$$

$$\begin{aligned} H_{\mathrm{v}}(\xi,\eta,\ell,d) \approx \sqrt{\frac{1}{N_{\mathrm{p}}}} \sum_{p\in\mathcal{B}_{\mathrm{v}}} \alpha_p f_{N_{\mathrm{R}}}(\xi/N_{\mathrm{R}} - \phi_{\mathrm{R},p}) f_{N_{\mathrm{T}}}^{*}(\eta/N_{\mathrm{T}} - \phi_{\mathrm{T},p}) \\ \mathrm{sinc}(d - T\nu_p, \ell - W\tau_p). \end{aligned} \tag{3.11}$$

The set $\mathcal{B}_{\mathrm{v}}$ partitions the N_{p} paths into a 4-D resolution cell of size $\Delta\tau \times \Delta\nu \times \Delta\phi_{\mathrm{T}} \times \Delta\phi_{\mathrm{R}}$ [41]. The maximum number of delay resolution bins is $L = \lceil W\tau_{\max} \rceil + 1$, where $\tau_{\max}$ represents the maximum delay spread during the CPI. Similarly, we can define the maximum number of resolvable (one-sided) Doppler shifts $D = \lceil T\nu_{\max}/2 \rceil$, where $\nu_{\max}$ represents the maximum Doppler spread during the CPI. Therefore, instead of representing the channel using actual delay, Doppler and AoD/AoA, the virtual channel is represented by uniform spaced delays $\tau_\ell = \ell/W$, Doppler shifts $\nu_d = d/W$, AoDs $\phi_{\mathrm{T},\eta} = \eta/N_{\mathrm{T}}$, and AoAs $\phi_{\mathrm{R},\xi} = \xi/N_{\mathrm{R}}$. The coefficients $\{H_{\mathrm{v}}(\xi,\eta,\ell,d)\}$ of the 4-D virtual channel data cube approximates the linear channel $\mathbf{H}_{\mathrm{p}}(t,f)$ using smoothing Dirichlet kernels $f_{N_{\mathrm{R}}}(\phi_{\mathrm{R}})$ and $f_{N_{\mathrm{T}}}(\phi_{\mathrm{T}})$, $f_{\mathrm{N}}(\phi) = (1/N)\sum_{i=0}^{N-1} e^{-j2\pi i\phi}$, and 2-D sinc kernel $\mathrm{sinc}(x,y) = e^{-j\pi x}\sin(\pi x)\sin(\pi y)/(\pi^2 xy)$. The extension to 2-D

arrays is straightforward by taking $\theta_{\mathrm{T},p}$ and $\theta_{\mathrm{R},p}$ under consideration [45, 46]. In numerical simulations, we have considered a uniform planar array (UPA) to characterize the performance of IEEE 802.11ad V2V-radar.

In the two-way radar channel, we consider that each virtual channel coefficient corresponding to $(\xi, \eta, \ell, d)^{\text{th}}$ cell, i.e., $\{H_{\mathrm{v,rad}}(\mathbf{\Lambda})\}$ is comprised of contributions from the reflections from the target vehicle, i.e., $h_0(\mathbf{\Lambda}_0)$ with $\mathbf{\Lambda}_0 = \{\xi_0, \eta_0, \ell_0, d_0\}$ that corresponds to the cell that containing $\{180^0 + \phi_0, \phi_0, \rho_0, \nu_0\}$, and from the surrounding clutter, i.e., $H_{\mathrm{c}}(\mathbf{\Lambda})$. We can, therefore, represent the radar virtual channel coefficient $H_{\mathrm{v,rad}}(\mathbf{\Lambda})$ as

$$H_{\mathrm{v,rad}}(\mathbf{\Lambda}) = \begin{cases} h_0(\mathbf{\Lambda}_0) + H_{\mathrm{c}}(\mathbf{\Lambda}_0) & \text{target present} \\ H_{\mathrm{c}}(\mathbf{\Lambda}) & \text{no target present} \end{cases} \tag{3.12}$$

If a dominant scatter is present at the $\mathbf{\Lambda}^{\text{th}}$ cell, then we assume that $H_{\mathrm{v,rad}}(\mathbf{\Lambda})$ is Rician distributed with deterministic LOS path, else we assume it is Gaussian distributed [29]. Since $h_0(\mathbf{\Lambda}_0)$ is the small-scale fading of the dominant LOS path corresponding to the target vehicle, it is assumed to be deterministic. Similarly, in case of dominant clutter scatter, $H_{\mathrm{c}}(\mathbf{\Lambda})$ is assumed to be Rician distributed, else it is assumed to be Gaussian distributed.

3.4 Beamforming

IEEE 802.11ad supports multiple antenna communication with a single data stream. Spatial multiplexing as found in IEEE 802.11n/ac is not supported. Therefore, we incorporate the TX/RX analog beamforming vectors into the baseband model even though the actual beamforming may happen

at an intermediate frequency (IF) or radio frequency (RF). The transmitted signal from the source vehicle at time t can be represented as

$$\mathbf{x}_{\mathrm{w}}(t) = \mathbf{f}_{\mathrm{T}} x(t), \tag{3.13}$$

where $\mathbf{f}_{\mathrm{T}} \in \mathbb{C}^{N_{\mathrm{T}} \times 1}$ is the TX analog beamforming vector at the source vehicle and $x(t)$ is defined in (3.1).

We assume that the source vehicle attempts to align its TX/RX beams towards the target vehicle using the IEEE 802.11ad beam training approach while establishing the communication link between them. Hence, once the link has been established, the TX and RX beams of the source vehicle are assumed to be pointing towards the $(\phi_0, 180^0 + \phi_0)$ direction with a small beam alignment error which is assumed to be within the resolution cell of the 4-D data cube in (3.8). At the same time, the RX beam of the target vehicle will also point towards the ϕ_0 direction to receive the V2V communication signal from the source vehicle, as shown in Fig. 3.3.

Assuming fixed beamforming for a CPI duration, the effective radar/ communication channel combined with TX and RX beamforming would result in

$$H_{\mathrm{w}}(t,f) = \mathbf{f}_{\mathrm{R}}^{*} \sum_{\xi=1}^{N_{\mathrm{R}}} \sum_{\eta=1}^{N_{\mathrm{T}}} \sum_{\ell=0}^{L-1} \sum_{\nu=-D}^{D} H_{\mathrm{v}}(\xi,\nu,\ell,d) \mathbf{a}_{\mathrm{R,v}}\left(\frac{\xi}{N_{\mathrm{R}}}\right) \mathbf{a}_{\mathrm{T,v}}^{*}\left(\frac{\eta}{N_{\mathrm{T}}}\right) \mathbf{f}_{\mathrm{T}} \; e^{-j2\pi \frac{\ell}{W} f} e^{j2\pi \frac{d}{T} t} \tag{3.14}$$

where $\mathbf{f}_{\mathrm{R}} \in \mathbb{C}^{N_{\mathrm{R}} \times 1}$ denotes the RX analog beamforming vector.

The beamforming vectors $\mathbf{f}_{\mathrm{T}}$ and $\mathbf{f}_{\mathrm{R}}$ at the source vehicle depend on ξ_0 corresponding to the target vehicle and can be represented as

$$\mathbf{f}_{\mathrm{T}} = \mathbf{a}_{\mathrm{T,v}}\left(\frac{\xi_0}{N_{\mathrm{T}}}\right), \tag{3.15}$$

$$\mathbf{f}_{\mathrm{R,com}} = \mathbf{a}_{\mathrm{R,v}}\left(\frac{\xi_0}{N_{\mathrm{R}}}\right). \tag{3.16}$$

where $\mathbf{f}_{\mathrm{R,com}}$ denotes the RX analog beamforming vector at the target vehicle. We assume that both at the source and the target vehicles, same IEEE 802.11ad-based beamforming codebook is used. Therefore, the RX beamforming at the source vehicle can be represented as

$$\mathbf{f}_{\mathrm{R,rad}} = \mathbf{f}^{\mathrm{c}}_{\mathrm{R,com}}. \tag{3.17}$$

The effective radar channel combined with TX and RX beamforming will be represented by

$$H_{\mathrm{w,rad}}(t,f) = \begin{cases} h_0(\mathbf{\Lambda}_0)e^{-j2\pi\frac{\ell_0}{W}f}e^{j2\pi\frac{d_0}{T}t} + h_{\mathrm{c}}(t,f) & \text{target present} \\ h_{\mathrm{c}}(t,f) & \text{no target present} \end{cases} \tag{3.18}$$

where $h_{\mathrm{c}}(t,f) = \sum_{\xi=1}^{N_{\mathrm{R}}}\sum_{\eta=1}^{N_{\mathrm{T}}}\sum_{\ell=0}^{L-1}\sum_{\nu=-D}^{D}\mathbf{f}_{\mathrm{R}}^{*}\mathbf{a}_{\mathrm{R,v}}\left(\frac{\xi}{N_{\mathrm{R}}}\right)\mathbf{a}_{\mathrm{T,v}}^{*}\left(\frac{\eta}{N_{\mathrm{T}}}\right)\mathbf{f}_{\mathrm{T}}H_{\mathrm{c}}(\xi,\nu,\ell,d)$ $e^{-j2\pi\frac{\ell}{W}f}e^{j2\pi\frac{d}{T}t}$ represents the clutter coefficient after incorporating the TX/RX beamforming. To simplify further theoretical analysis of the proposed radar processing techniques, we have assumed $h_{\mathrm{c}}(t,f)$ is Gaussian distributed, which will cover the case of non-dominant clutter [29], residue left after dominant clutter cancellation [47], and worst case analysis for dominant clutter. In numerical simulations, however, we have also considered the more general case of multi-path channel with non-Gaussian distributed clutter for the sake of completeness.

3.5 Received Signal

We apply the stop-and-hop assumption to model the round-trip delay and phase modulation in a time-varying echo signal [38]. Under this assumption, the echo is received with a time delay corresponding to the range at the beginning of the pulse transmission but with a phase modulation related to the time variation in range. Then, the received signal at the source vehicle for a CPI would result in

$$y(t) = \sqrt{\mathcal{E}_{\mathrm{s}} G_{\mathrm{rad}}} g_{\mathrm{R}}(t) * h_0(\mathbf{\Lambda}_0) x(t - \ell_0/W) e^{j2\pi \frac{d_0}{T} t} + z_{\mathrm{c}}(t) + z_{\mathrm{n}}(t) + z_{\mathrm{I}}(t) + z_{\mathrm{FD}}(t), \tag{3.19}$$

where G_{rad} denotes the large-scale radar channel gain, which is given by the free-space path-loss model as [21, 30, 48]

$$G_{\mathrm{rad}} = \frac{G_{\mathrm{T}} G_{\mathrm{R}} \lambda^2 \sigma_{\mathrm{RCS}}}{(4\pi)^3 \rho_0^4}, \tag{3.20}$$

where σ_{RCS} is the radar cross section corresponding to the target vehicle, while the discretized delay, ℓ_0 and the discretized Doppler shift, d_0, satisfies the relation

$$\ell_0/W - \Delta\tau/2 < \tau_0 < \ell_0/W + \Delta\tau/2, \tag{3.21}$$

$$d_0/T - \Delta\nu/2 < \nu_0 < d_0/T + \Delta\nu/2. \tag{3.22}$$

In (3.19), $z_{\mathrm{n}}(t)$ is additive white Gaussian noise (AWGN) with power σ_{n}^2, $z_{\mathrm{I}}(t)$ is the received interference signal at the source vehicle due to the transmitted signals from other surrounding vehicles, $z_{\mathrm{FD}}(t)$ is the self-interference factor due to the full-duplex assumption at the source vehicle, and $z_{\mathrm{c}}(t) = g_{\mathrm{R}}(t) *$

$\sqrt{\mathcal{E}_{\mathrm{s}}G_{\mathrm{c}}}h_{\mathrm{c}}(t,f)*x(t)$ is the non-dominant clutter with large-scale clutter channel gain G_{c}. The non-dominant clutter, $z_{\mathrm{c}}(t)$, is assumed to be distributed as $\mathcal{CN}(0,\sigma_{\mathrm{c}}^2)$.

We assume that the full-duplex system we are using has a good enough self-interference cancellation mechanism with an efficient circulator [49], and the possibility of spacing between the transmit and receive arrays. Therefore, we can ignore self-interference effects inherent in the joint radar and communication system. Since the radar waveform is IEEE 802.11ad-based, there will be a coordinated directional transmission by a personal basic service set control point, which would mitigate inter-user interference. Therefore, the discrete-time representation of the received signal in (3.19) is

$$Y[k,m]=\sqrt{\mathcal{E}_{\mathrm{s}}G_{\mathrm{rad}}}h_0(\mathbf{\Lambda}_0)S[k-\ell_0,m]e^{j2\pi\frac{d_0}{T}(k+mK)T_{\mathrm{s}}}+Z_{\mathrm{c}}[k,m]+Z_{\mathrm{n}}[k,m], \tag{3.23}$$

where $S[k,m]=\sum\limits_{n}s[k+mK]g(((k+mK)-n)T_{\mathrm{s}})$, $g(t)=g_{\mathrm{R}}(t)*g_{\mathrm{T}}(t)$, $Z_{\mathrm{c}}[k,m]=z_{\mathrm{c}}((k+mK)T_{\mathrm{s}})$, and $Z_{\mathrm{n}}[k,m]=z_{\mathrm{n}}((k+mK)T_{\mathrm{s}})$.

Since the TX and RX pulse shaping filters lead to an equivalent filter verifying the Nyquist condition, then $g(nT_{\mathrm{s}})=\delta[n]$ and $S[k,m]=s[k+mK]$. Therefore, we can represent the received signal corresponding to the m^{th} frame as

$$\mathbf{y}_m=\sqrt{\mathcal{E}_{\mathrm{s}}G_{\mathrm{rad}}}h_0(\mathbf{\Lambda}_0)e^{j2\pi\frac{d_0}{M}m}\mathbf{F}\mathbf{s}_m+\mathbf{z}_m, \tag{3.24}$$

where $\mathbf{y}_m\in\mathbb{C}^{K\times 1}$ and $\mathbf{x}_m\in\mathbb{C}^{K\times 1}$ represent the received and transmitted samples with $y_m[k]=Y[k,m]$ and $s_m[k]=X[k-\ell_{\mathrm{u}},m]$, respectively. The

vector $\mathbf{z}_m \in \mathbb{C}^{K\times 1}$ represents the clutter-plus-noise vector satisfying the relation $z_m[k] = Z_{\rm c}[k,m] + Z_{\rm n}[k,m]$ with distribution $\mathcal{CN}(0,\sigma_{\rm cn}^2)$, where $\sigma_{\rm cn}^2 = \sigma_{\rm c}^2 + \sigma_{\rm n}^2$. The Doppler shift matrix $\mathbf{F}$ is a $K \times K$ diagonal matrix given by $\mathbf{F} = \text{diag}(1, e^{j2\pi d_0/KM}, \cdots, e^{j2\pi d_0(K-1)/KM})$ [41]. The SCNR of the received radar signal can, therefore, be defined as $\mathcal{E}_{\rm s}G_{\rm rad}/\sigma_{\rm cn}^2$.

For each frame, the phase shift d_0k/KM corresponding to the training sequence is very small and therefore, we can assume the channel to be time invariant [41]. The simplified signal model corresponding to the received training sequence of the $k^{\rm th}$ symbol in the $m^{\rm th}$ frame can be represented as

$$y_m[k] = \sqrt{\mathcal{E}_{\rm s}G_{\rm rad}}h_0(\mathbf{\Lambda}_0)e^{j2\pi\frac{d_0}{M}m}s[k-\ell_0] + z_m[k], \tag{3.25}$$

where the transmitted symbol corresponding to the preamble in all the frames are the same, i.e., $x[k-\ell_0] = X[k-\ell_0, m]$ across all the M frames.

Similar to the received radar signal model developed at the source vehicle, we can represent the received communication signal at the target vehicle as

$$Y_{\rm com}[k,m] = \sqrt{\mathcal{E}_{\rm s}G_{\rm com}}h_{\rm com}[k,m]S[k-\ell_{\rm com}/W, m]e^{j2\pi\frac{d_{\rm com}}{T}(k+mK)T_{\rm s}} + Z_{\rm com}[k,m], \tag{3.26}$$

where $h_{\rm com}[k,m]$ is the small-scale channel fading, $\ell_{\rm com}/W - \Delta\tau/2 < \tau_{\rm com} < \ell_{\rm com}/W + \Delta\tau/2$, $d_{\rm com}/T - \Delta\nu/2 < \nu_{\rm com} < d_{\rm com}/T + \Delta\nu/2$, $\tau_{\rm com} = \tau_0/2$ is the one-way communication path delay and $\nu_{\rm com} = -\nu_0$ is the Doppler shift corresponding to the relative velocity of the source vehicle with respect to the target vehicle and $Z_{\rm com}[k,m]$ is the AWGN noise, which is distributed

as $\mathcal{CN}(0, \sigma_{\mathrm{n}}^2)$. Since automotive radar uses a constant free-space path loss in (3.20) for a CPI, therefore, the complex communication channel gain at the target vehicle in the same CPI, G_{com}, is modeled using the free-space path-loss model as [50]

$$G_{\mathrm{com}} = \frac{G_{\mathrm{T}} G_{\mathrm{R}} \lambda^2}{(4\pi\rho_0)^2} = \frac{4\pi\rho_0^2}{\sigma_{\mathrm{RCS}}} G_{\mathrm{rad}}. \tag{3.27}$$

The SNR of the received communication signal can, therefore, be defined as $\mathcal{E}_{\mathrm{s}} G_{\mathrm{com}} / \sigma_{\mathrm{n}}^2$. Due to variability of small-scale fading with scatter distribution, location and orientation, it is reasonable to assume that the small-scale fading corresponding to the communication channel is independent of the small-scale fading corresponding to the radar channel and the receiver noise, i.e. $h_{\mathrm{com}}[k, m]$ is independent of $h_0(\mathbf{\Lambda}_0)$, $Z_{\mathrm{c}}[k, m]$ and $Z_{\mathrm{com}}[k, m]$. We also assume that the communication channel is Rician distributed with D_{com} as the Rice factor, due to the assumption of narrowband LOS dominated channel for two-way radar channel.

Chapter 4

Proposed Receiver Processing Techniques For Enabling Radar Functions

We consider three primary types of radar processing: 1) *vehicle detection* using a constant false alarm rate algorithm; 2) *range estimation* using a time synchronization technique; and 3) *velocity estimation* using a frequency synchronization technique. The radar processing exploits the special structure of GCP/GCS in the preamble of 802.11ad frames and leverages the communication preprocessing to detect and estimate its parameters of interest, as shown in Fig. 4.1. Indeed, the algorithms used in the radar module are based on the pulse-Doppler radar processing and developed by extending the methods used in communication techniques over a single frame to multiple frames [51]. This approach enables the realization of a joint vehicular communication and radar paradigm using a conventional low-cost IEEE 802.11ad scheme with minimal receiver modifications.

4.1 Training Sequence Processing Per Frame in the Communication Module

In IEEE 802.11ad, the training sequences of a single frame are used for time and frequency synchronization and channel estimation. This is achieved

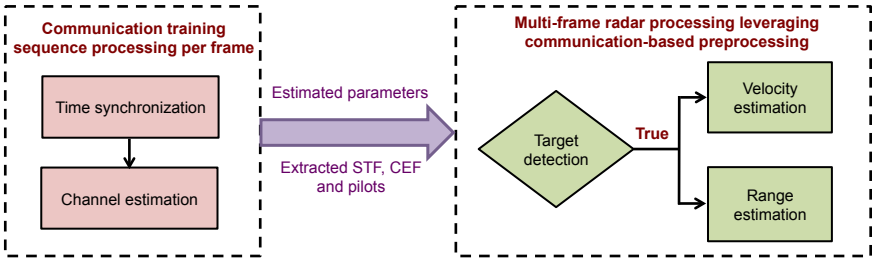

Figure 4.1: The flowchart represents the processing techniques for target detection and range/velocity estimation using IEEE 802.11ad V2V-radar. The processing techniques leverage the special structure of GCS and GCP present in the STF and the CEF of multiple frames in one CPI for desired automotive radar performance.

in several steps: 1) *coarse time synchronization* based on preamble detection techniques using the STF; 2) *frequency offset estimation* using the STF; 3) *fine time synchronization* using the CEF symbol boundary detection and the STF/CEF peak detection techniques; and 4) *channel estimation* using the CEF. Since we assume the channel to be frequency flat for a single frame duration, we do not perform frequency synchronization in communication processing module. We, however, estimate the Doppler shift in the velocity estimation module using multiple frames.

The first step of the preprocessing is to detect the IEEE 802.11ad frame using the STF. The frame start detection technique applies a threshold $\chi_{\mathrm{STF}} < 1$ on the normalized auto-correlation to coarsely estimate the starting sample of the preamble [52]. The k^{th} normalized auto-correlation corresponding to the m^{th} frame is given by

$$R_1[\ell, m] = \frac{\sum_{n=0}^{P-1} y_m[\ell - n] y_m^*[\ell - n - N_{\mathrm{D}}]}{\sqrt{\sum_{n=0}^{P-1} |y_m[\ell - n]|^2} \sqrt{\sum_{n=0}^{P-1} |y_m^*[\ell - n - N_{\mathrm{D}}]|^2}}, \tag{4.1}$$

where $P = 128$ is the length of the training sequence and $N_{\mathrm{D}} = 128$ is the distance between the two training sequences chosen for correlation. The coarse target range estimate of the target vehicle by applying the preamble start detection technique to the m^{th} frame is given by

$$\hat{\ell}_{01}[m] = \inf\left\{\ell \mid R_1[\ell, m] \geq \chi_{\mathrm{STF}}\right\}. \tag{4.2}$$

The fine range estimate of the time-delay can be obtained either by using an amplitude-based method or a phase-based method. The amplitude-based method estimates the fine time-delay, $\hat{\ell}_{02}[m]$, by detecting the peaks of cross-correlation between $\mathbf{Ga}_{128}$ and multiple GCSs in the STF sequence [52]. Here,

$$\hat{\ell}_{02}[m] = \underset{\ell:\ell\in\mathbb{Z}}{\arg\max}\, |R_2[\ell, m]|^2, \tag{4.3}$$

where,

$$R_2[\ell, m] = \sum_{i=0}^{P_{\mathrm{r}}-1} \sum_{n=0}^{P-1} Ga_{128}[n] y_m[\ell + n + iP], \tag{4.4}$$

$\mathbb{Z}$ is the set of integers, $P = 128$, and $P_{\mathrm{r}} = 16$ is the number of repetitions of $\mathbf{Ga}_{128}$ in the STF. The amplitude-based fine timing synchronization can also be similarly performed by applying the peak detection technique on the CEF instead of the STF. Both the peak detection methods perform well at low SNR of the received communication signal.

The timing synchronization at the m^{th} frame can also be fine tuned by performing phased-based symbol boundary detection using the auto-correlation

defined as [52]:

$$R_3[\ell, m] = \sum_{n=0}^{P-1} y_m[\ell - n] \times (y_m^*[\ell - n - 2P] + y_m^*[\ell - n - 4P]), \tag{4.5}$$

where $P = 32$ is the length of each of the four Golay sequences that comprise $\mathbf{Ga}_{128}$. At the end of the STF field, there is $-\mathbf{Ga}_{128}$. This causes a phase inversion in the correlation result, as described in [52]. As a result, the delay can be estimated by detecting the sample number where the phase inversion appears. The boundary $\hat{\ell}_{03}[m]$ of the CEF field is defined as the sample number which is $2P$ samples before the phase inversion, i.e.,

$$\hat{\ell}_{03}[m] = \inf \{\ell - 2P \mid \text{sgn}(\angle R_3[\ell, m])\text{sgn}(\angle R_3[\ell + 1, m]) = -1\}, \tag{4.6}$$

where $\text{sgn}(\cdot)$ is the sign operator and a peak occurs at $\hat{\ell}_3[m]$. This method, however, does not perform well in the presence of Doppler shift at low SNR of the received communication signal.

After the fine time synchronization, we extract the received CEF signal to estimate the channel using a 512 sample GCP. The equation to be implemented to obtain an estimate of the channel using a Golay correlator is expressed as

$$\hat{\gamma}(\mathbf{y}_m, \ell) = \frac{1}{2P} \left(\sum_{n=0}^{P-1} y_m[n + \ell] G u_{512}^*[n] + \sum_{\ell=0}^{P-1} y_m[n + \ell + P] G v_{512}^*[n] \right) \tag{4.7}$$

and hence, our channel estimate corresponding to the m^{th} frame, $\hat{\mathbf{h}}_m \in \mathbb{C}^{P \times 1}$, is

$$\hat{h}_m[\ell] = \hat{\gamma}(\mathbf{y}_m, \ell + N_{\text{CP}}) \quad \ell = 0, \cdots, P - 1, \tag{4.8}$$

where $P = 512$ and the length of the cyclic prefix $N_{\mathrm{CP}} = 128$. The channel estimate can also be written as

$$\hat{h}_m[\ell] = \begin{cases} \sqrt{\mathcal{E}_{\mathrm{s}} G_{\mathrm{rad}}} h_u e^{-j2\pi \frac{d_0}{M} m} + \tilde{z}_m[\ell] & \ell = \ell_{\mathrm{CES}} \\ \tilde{z}_m[\ell] & \text{otherwise} \end{cases} \tag{4.9}$$

where $\tilde{z}_m[\ell] = \hat{\gamma}(\mathbf{z}_m, \ell + N_{\mathrm{CP}})$ and $\ell_{\mathrm{CES}} = 256$. Note that $\mathbf{z}_m$ represents the clutter-plus-noise vector as defined in (3.24).

4.2 Target Vehicle Detection

The target vehicle is detected using the constant false alarm (CFAR) detection based on the typical WLAN non-zero channel tap detection [53]. In this technique, the decision is based on a simple thresholding function

$$\varphi(\sqrt{\mathcal{E}_{\mathrm{rad}}}) = \begin{cases} 0 & \text{if } \mathcal{E}_{\mathrm{rad}} < \chi_{\mathrm{D}} \\ 1 & \text{if } \mathcal{E}_{\mathrm{rad}} > \chi_{\mathrm{D}} \end{cases} \tag{4.10}$$

where $\mathcal{E}_{\mathrm{rad}} = \mathcal{E}_{\mathrm{s}} G_{\mathrm{rad}} |h_u|^2$. For a constant false alarm probability of P_{FA}, the detection threshold becomes [44]

$$\chi_{\mathrm{D}} = -\sigma_{\mathrm{cn}}^2 \ln P_{\mathrm{FA}}, \tag{4.11}$$

where σ_{cn}^2 is the variance of the zero-mean complex Gaussian clutter-plus-noise term $\tilde{z}_m[\ell]$. We assume that the value of σ_{cn}^2 is known because it can be easily calculated using the typical mmWave WLAN noise variance estimation technique [44, 53].

4.3 Velocity Estimation

The relative velocity of the target vehicle is estimated by calculating the Doppler frequency of the target echo and then estimating the velocity using (3.6). To estimate the Doppler shift corresponding to the target vehicle we will use the least squares (LS)-based frequency-offset estimation method over single/multiple frames. For this purpose, we will choose $\mathbf{p} \in \mathbb{C}^{PM\times 1}$ to be a vector of M slow time samples across P delay bins, i.e.,

$$\mathbf{p} = \begin{bmatrix} y_0[k_0] & y_0[k_1] & \cdots & y_0[k_{P-1}] \cdots y_{M-1}[k_0] & y_{M-1}[k_1] & \cdots & y_{M-1}[k_{P-1}] \end{bmatrix}, \tag{4.12}$$

where $\{k_i \mid 0 \leq i \leq P-1\}$ is an index set for the samples across fast time axis and it corresponds to the location of the training sequences in each frame.

The Doppler frequency estimation using Moose algorithm, described in [54], on a single frame does not achieve the desire velocity accuracy of 0.1 m/s, as shown in [15]. Therefore, to achieve desired velocity accuracy, we propose a multi-frame Moose-based algorithm for the Doppler frequency estimation problem as

$$\hat{\nu}_0 = \frac{\hat{d}_0}{T} = \frac{\angle\Big(\sum_{i=0}^{M-1}\sum_{n=0}^{P-1} p[n+N_{\mathrm{D}}+iP]p^*[n+iP]\Big)}{2\pi T_{\mathrm{D}}}, \tag{4.13}$$

where $\hat{d}_0$ is the discrete delay corresponding to τ_0, T is the CPI duration, N_{D} is the distance between two training sequences chosen for correlation, and T_{D} is the time interval between these two training sequences, which in case of a single frame is $N_{\mathrm{D}}T_{\mathrm{s}}$, and in case of multiple frames is the duration of the

frame, i.e., KT_{s}. The resolution and accuracy of frequency-offset estimation will improve when we use multiple frames (similar to pulse-Doppler radar) as compared to a single frame (traditionally used in frequency synchronization algorithms of a standard WLAN receiver) because of larger integration time.

Remark 1. The theoretical performances of the LS-based frequency-offset estimation in (4.13) for a single target vehicle with velocity v in a flat fading channel, as derived in Appendix-A, are:

- The velocity resolution is given by

$$\Delta v = \frac{\lambda}{2T_{\mathrm{int}}}, \tag{4.14}$$

  where T_{int} is the total integration time used for velocity estimation, which in case of a single frame is PT_{D} with $T_{\mathrm{D}} = T_{\mathrm{s}}$, and in case of multiple frames is MT_{D} with $T_{\mathrm{D}} = KT_{\mathrm{s}}$. Since, $K > P$ in SC PHY frames, therefore multiple frames have more T_{int} than a single frame. This implies that as the number of frames increases, the resolution of the velocity estimation increases.

- The CRLB bound for the velocity estimation using the STF of a single frame is

$$\sigma_{\hat{v}}^2 = \frac{6\lambda^2}{(4\pi)^2 P^3 T_{\mathrm{D}}^2 (\mathcal{E}_{\mathrm{rad}}/\sigma_{\mathrm{cn}}^2)}. \tag{4.15}$$

  The CRLB expresses a lower bound on the variance of velocity estimators using the STF of a single frame. If $\sigma_{\hat{v}}^2$ is above the LRR's desired

mean square error for velocity estimation, then it indicates that the requirement for LRR velocity accuracy cannot be met in any case. It can be inferred from (4.15) that the mean square error of the velocity estimation decreases rapidly with an increase in P. The value of P, however, is constant in a SC PHY frame, which implies the CRLB gets mainly affected by the change in SCNR.

- In case of multiple frames, the CRLB bound for velocity estimation using preamble across multiple frames for large M is

$$\sigma_{\hat{v}}^2 \approx \frac{6\lambda^2}{(4\pi)^2(MP^3 + M^3PK^2)T_{\mathrm{s}}^2(\mathcal{E}_{\mathrm{rad}}/\sigma_{\mathrm{cn}}^2)}. \tag{4.16}$$

  Similar to (4.15), (4.16) also suggests that velocity estimation accuracy increases with increase in number of preambles and SCNR. Unlike (4.15), however, (4.16) adds the flexibility of increasing the number of total preambles, i.e., MP, by choosing higher values of M, which increases the accuracy of the velocity estimation.

  The extra flexibility in varying M enables a system trade-off between target velocity estimation accuracy and communication data rate for the number of frames within a CPI. The accuracy of velocity estimation grows with an increase in the total training sequence duration and the numbers of frames within a fixed size CPI. This dependence can be seen using $\sigma_{\hat{v}}^2$ for the P sample preamble across variable number of frames, M, within a fixed size $T = MKT_{\mathrm{s}}$ duration CPI as

$$\sigma_{\hat{v}}^2 = \frac{6}{4\pi^2(MP^3 + M^3PK^2)T_{\mathrm{s}}^2(\mathcal{E}_{\mathrm{rad}}/\sigma_{\mathrm{cn}}^2)}. \tag{4.17}$$

The number of communication data symbols, however, decreases with an increase in the training sequence duration. We consider the following data rate as the performance metric of the communication system

$$R = \frac{MK_{\mathrm{CD}}T_{\mathrm{s}}}{T}\mathbb{E}\left[\log_2\left(1+\frac{\mathcal{E}_{\mathrm{com}}}{\sigma_{\mathrm{n}}^2}\right)\right] \tag{4.18}$$

or,

$$R = \frac{7}{8}\left(1-\frac{MPT_{\mathrm{s}}}{T}\right)\mathbb{E}\left[\log_2\left(1+\frac{\mathcal{E}_{\mathrm{com}}}{\sigma_{\mathrm{n}}^2}\right)\right], \tag{4.19}$$

where $\mathcal{E}_{\mathrm{com}} = \mathcal{E}_{\mathrm{s}}G_{\mathrm{com}}|h_{\mathrm{com}}[k,m]|^2$, K_{CD} is the total number of communication data symbols within a frame, which is $(7/8)^{\mathrm{th}}$ fraction of the $K-P$ symbols, because there is a 64 symbols guard interval after every 448 data symbols.

- Due to the periodicity of the exponential function, the estimate of the Doppler shift calculated in (4.13) will only be accurate for

$$|\hat{\nu}_0| \leq \frac{1}{2T_{\mathrm{D}}}. \tag{4.20}$$

Comparing (4.14), (4.15), (4.15) and (4.20), we infer that there is a the trade-off between accuracy/resolution and the span of unambiguous velocity estimation. If the distance between two consecutive training sequences increases, then the velocity estimation becomes more accurate with higher resolution. It, however, will decrease the span of unambiguous velocity estimation.

4.4 Range Estimation

Once the target vehicle is detected, the range of the target cell from the source vehicle is calculated from (3.5) by estimating the corresponding delay-shift. The range estimation algorithms are applied on the STF and the CEF and can be categorized into two main types: coarse range estimation, using a frame start detection estimate $\hat{\ell}_{01}[m]$ with an error of less than 128×3 samples [52], and fine range estimation based on symbol boundary detection, and the STF/CEF peak detection technique based on $\hat{\ell}_{02}[m]$ and $\hat{\ell}_{03}[m]$ with an error less than 1 sample [52], which meets the LRR specifications of 0.1 m range accuracy [12].

Remark 2. The range resolution for the signal model expressed in (3.25) for a given training sequence is [55]

$$\Delta\rho = \frac{c}{2W_{\text{rms}}} \leq \frac{c}{2W}, \tag{4.21}$$

where W_{rms} is the root-mean square (RMS) bandwidth defined as

$$W_{\text{rms}} = \sqrt{\frac{\int_{-\infty}^{\infty}(2\pi f)^2|X(f)|^2df}{\int_{-\infty}^{\infty}|X(f)|^2df}} \tag{4.22}$$

and $X(f)$ represents the Fourier transform of $x(t)$ over the duration of the given training sequence. The CRLB bound of the range estimation using IEEE 802.11ad preamble can be expressed as [55, 56]

$$\sigma^2_{\hat{\rho}} = \frac{c^2}{32\pi^2 W^2_{\text{rms}}\mathcal{E}_{\text{rad}}/\sigma^2_{\text{cn}}} \leq \frac{c^2}{32\pi^2 W^2\mathcal{E}_{\text{rad}}/\sigma^2_{\text{cn}}}. \tag{4.23}$$

For SCNR above 0 dB and $W = 2.16$ GH, it can be calculated from the theoretical bounds in (4.21) and (4.23) that it is possible to achieve cm-level resolution/accuracy using a single frame of IEEE 802.11ad. In numerical results, we will show that using the time-delay estimate calculated via communication-based processing, we can achieve the desired range resolution/accuracy of ≤ 0.1 m.

Chapter 5

Numerical Results

In this chapter, we perform Monte-Carlo simulations with 10,000 trials to evaluate the proposed radar techniques using IEEE 802.11ad against the required system specifications for LRR in a typical automotive radar setting [12, 57]. We consider the transmit and receive pulse shaping filters as root-raised cosine with a roll-off factor of 0.25 and the radar cross section as 10 dBsm [21]. The multiple antenna system is assumed to be a UPA with 8 horizontal and 2 vertical elements, with a 3 dB horizontal beamwidth of 13^o and a vertical beamwidth of 60^o [24–26].

The metric used to compare the performance of different estimation algorithms is the mean square error (MSE), defined as

$$\text{MSE} = \mathbb{E}\left[|\hat{\gamma} - \gamma|^2\right], \tag{5.1}$$

where γ is the true value of the parameter and $\hat{\gamma}$ is the estimated value. The metric used to evaluate the detection performance of the IEEE 802.11ad V2V-radar is the probability of detection P_{D} for different probabilities of false alarms, and is given by the fraction of successful target detections when a target is present, i.e.,

$$P_{\text{D}} = \mathbb{E}[\varphi(\sqrt{\mathcal{E}_{\text{rad}}}) \mid \text{target present}], \tag{5.2}$$

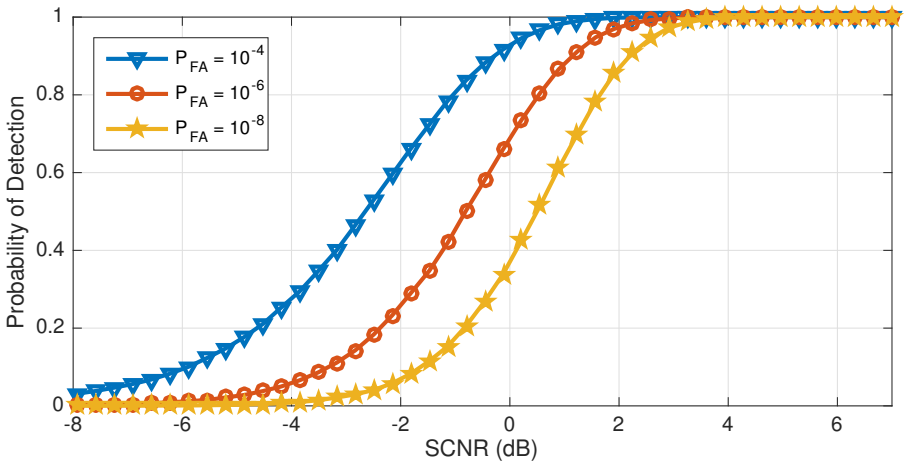

Figure 5.1: Probability of detection using different constant false alarm detection rates.

where $\varphi(\sqrt{\mathcal{E}_{\text{rad}}})$ is defined in (4.10).

5.1 Detection and Estimation Accuracy in Typical Automotive Scenario

For the complex Gaussian distributed clutter-plus-noise scenario, we randomly chose the distance and the relative speed between the target vehicle and the source vehicle as 50 m and 20 m/s, which falls in the typical span of LRR range and velocity specifications [57]. We assume that the TX and the RX beams are pointed towards the target vehicle after the IEEE 802.11ad beam alignment process.

Fig. 5.1 shows the probability of detection P_{D} using different false alarm probabilities. It indicates that P_{D} grows with increasing P_{FA}. For a P_{FA} of 10^{-4}, we achieve radar detection rates greater than 90% above the received

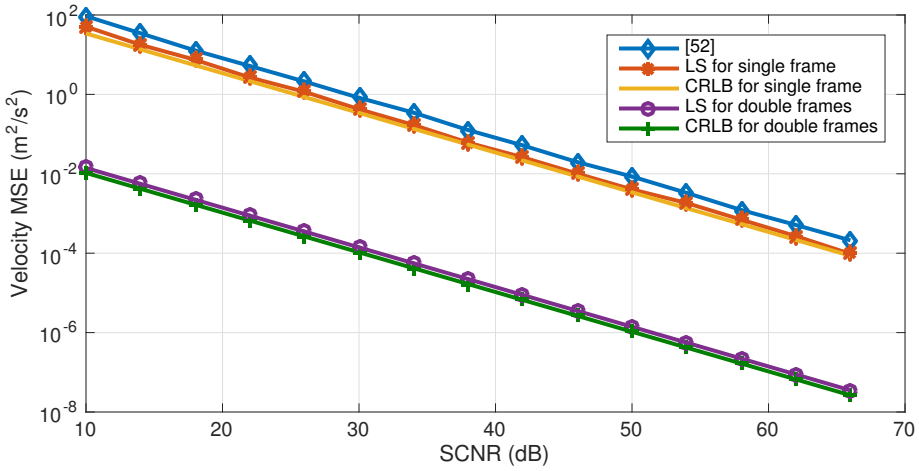

Figure 5.2: MSE of the velocity estimation using the STF of a single and the preamble of the double frames. The numerical results of proposed estimation techniques closely match to the CRLB bounds.

SCNR of 0 dB.

Fig. 5.2 shows MSE of the estimated relative velocity using the STF of a single frame with $P = 128 \times 16$ and $N_{\mathrm{D}} = 512$, and using the preamble of two frames with $P = 128 \times 26$ and $N_{\mathrm{D}} = 41285$. The performances of velocity estimation techniques increase linearly (in dB scale) with the SCNR. The LS-based estimation technique is comparatively better than the one proposed in [52]. The accuracy of LS-based estimation techniques is very close to its CRLB bounds. Using double frames we achieve much better velocity estimation accuracy than using a single frame for all SCNR values. At low SCNR (less than 10 dB), however, even using double frames we do not achieve the desired velocity accuracy of 0.1 m/s.

This motivates us to exploit multiple frames as explained in chapter

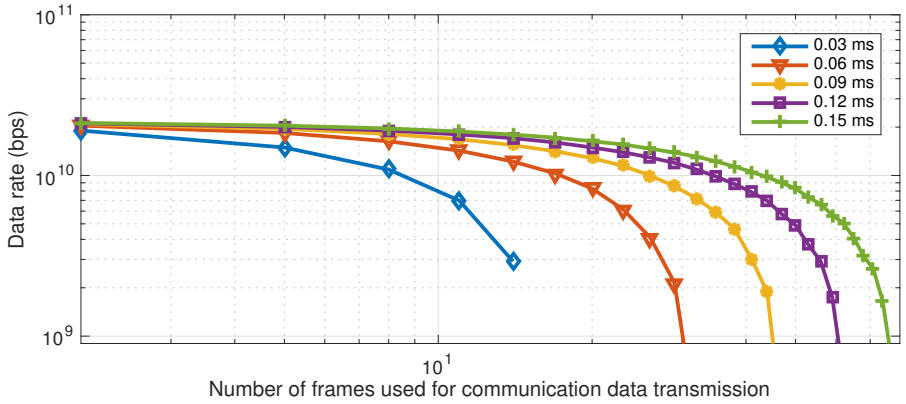

(a) Data rate of the IEEE 802.11ad system for a fixed duration of CPI

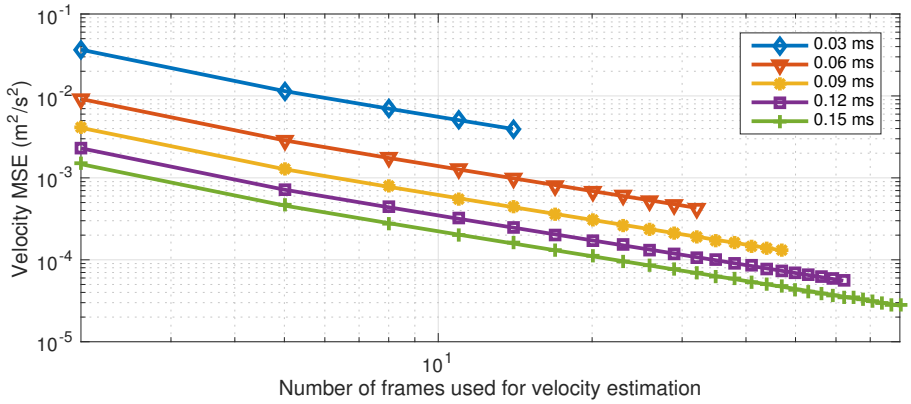

(b) MSE of the velocity estimation using multiple frames for a fixed size CPI

Figure 5.3: Trade-off between communication data rate and velocity estimation for a fixed size CPI. By increasing the duration of training symbols within a CPI, velocity estimation becomes more accurate with reduced data rate.

4.3, which inherently increases the training sequence and frame duration to better estimate velocity using the LS-based method. The performance of this algorithm, however, depends on the number of frames that can be used in a CPI.

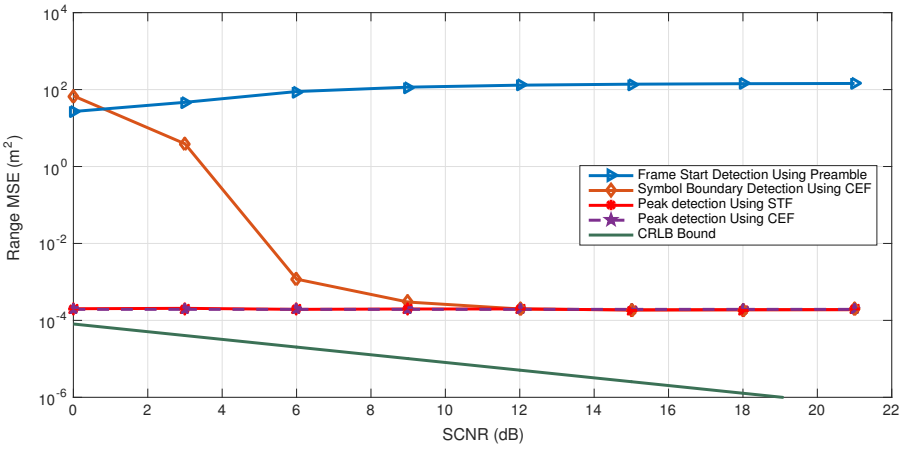

Figure 5.4: MSE of the range estimation using the preamble in a single frame based on coarse and fine range estimation algorithms.

To evaluate the dependence of velocity estimation on the number of frames within a CPI and investigate its simultaneous effect on the communication data rate of the system, we have performed simulations over several CPI intervals with varying number of frames at 10 dB SCNR, as shown in Fig. 5.3. For a fixed CPI duration, the number of frames is varied from one to its maximum limit within a CPI. We observe from the simulations that as the number of frames increases within a fixed CPI, the communication data rate degrades while enhancing the velocity estimation accuracy. In spite of this trade-off, we observe that it is indeed possible to achieve Gbps communication data rate and cm/s-level accurate target velocity estimation simultaneously for a CPI of 0.06 ms or more.

In Fig. 5.4, we compare the performance of various proposed range estimation algorithms and the CRLB bound using a single frame. The desired

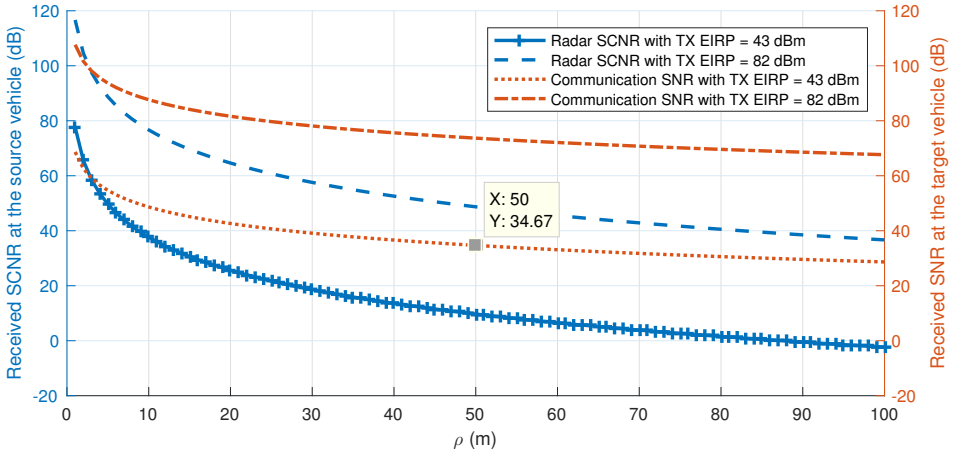

Figure 5.5: Received radar SCNR at the source vehicle and received communication SNR at the target vehicle as a function of distance between the source and the target vehicle.

range MSE for automotive radars is 0.01m. For frame start detection using the STF we chose a threshold of $\chi_{\text{STF}} = 1/8$ [52]. We observe from Fig. 5.4 that the fine range estimation achieves the desired accuracy using the STF/CEF peak detection for SCNR above 0 dB, and using the CEF symbol boundary detection for SCNR above 6 dB. The poor performance of range estimation using the CEF symbol boundary detection at low SCNR can be attributed to the fact the performance of the phase-based estimation gets affected by Doppler shift. The figure also shows that the performance of the frame start detection using the preamble degrades due to a constant threshold χ_{STF}, which does not adapt to the increasing SCNR. The amplitude-based peak detection technique using the STF/CEF, however, meets the desired automotive range accuracy of 0.1 m using a single frame without incorporating significant complexity.

Fig. 5.5 shows that the received radar SCNR at the source vehicle and

received communication SNR at the target vehicle decreases with increasing distance between the source and the target vehicle for a given TX equivalent isotropically radiated power (EIRP) of 43 dBm (maximum EIRP for indoor applications [17]) and 82 dBm (average EIRP for 60 GHz devices with antennas located outdoors [58]). We also infer from Fig. 5.5 that for a give EIRP, one way received communication SNR is higher than the radar SCNR for a given EIRP for the channel gains defined in (3.20) and (3.27).

5.2 Resolution and Robustness to Dominant Clutter

The performance of the IEEE 802.11ad V2V-radar is also evaluated for the case when the clutter is dominant, making the distribution of the clutter-plus-noise ratio Rician [59]. This scenario will unfold interesting characteristics of the system, such as its range and velocity resolutions. For this purpose, we chose a scenario with another remote vehicle in the surrounding of the target vehicle. The relative velocity of the target vehicle is 30 m/s less than that of the clutter vehicle. The clutter vehicle is 8.02 m closer to the source vehicle than the target vehicle. The azimuth angle of the the target vehicle is 30^o and the clutter vehicle is 20^o. The TX and RX beams of the source vehicle point at 30^o, the direction of the target vehicle.

Figs. 5.6 and 5.7 represent the 2-D and 3-D plot of the matched filtered received signal in the range and Doppler domains with 10 frames in one CPI of 128000 samples, i.e., 0.072 ms duration. The size of each range resolution cell is 0.08 m and the size of each Doppler resolution cell is 13750

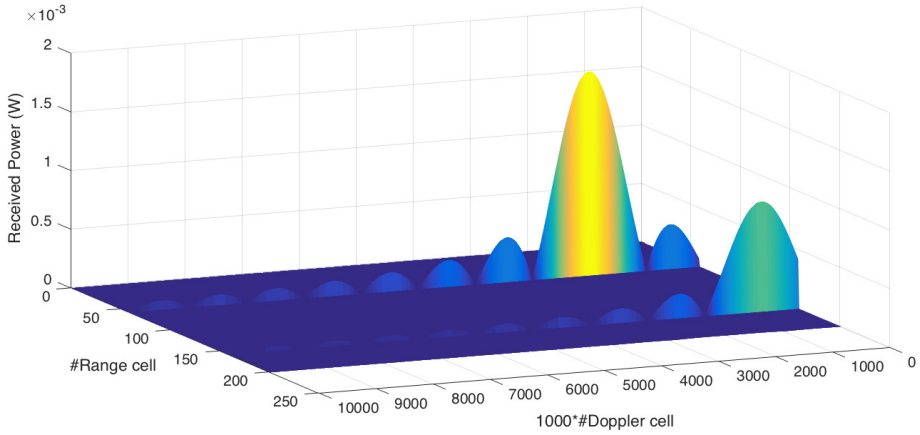

Figure 5.6: The mesh plot of the matched filtered received signal in the range and the Doppler domains. The plot shows two mainlobe peaks corresponding to the simulated target and clutter vehicles with range of 4.64 m and 12.65 m and velocity of 30 m/s and 60 m/s, respectively. Due to the broad mainlobe width in the Doppler domain velocity resolution is limited to around 35 m/s in this simulation.

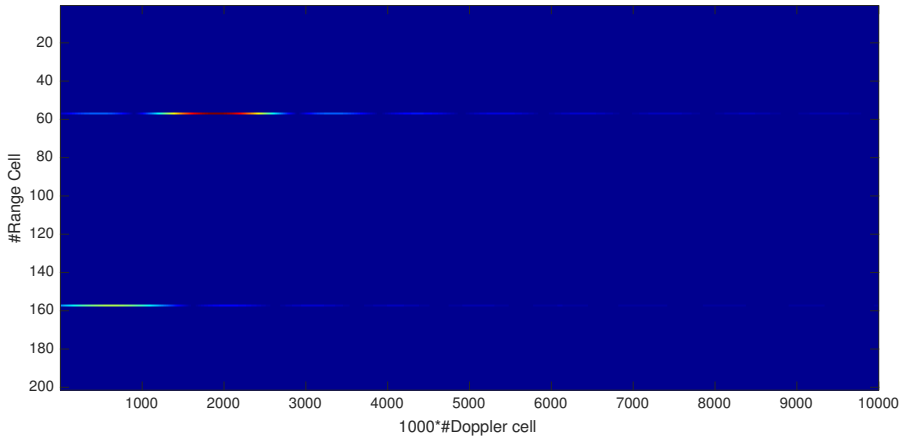

Figure 5.7: The 2D-plot of the matched filtered received signal in the range and the Doppler domain shows that there are two targets present in the 58^{th} and 158^{th} range cells and in the first and second Doppler resolution cells.

KHz, calculated from (4.21) and (A.11), respectively. In both figures, we plot the matched received filter amplitude with respect to the range cell and 1000 times interpolated Doppler cell. The Doppler cell is interpolated to visualize the resolution degradation effect due to the wide mainlobe and high sidelobes of the Doppler response in a given range bin (cells corresponding to the same delay bin). These plots show that the target and clutter responses are separated by 100 range cells, corresponding to 8 m. The matched filter response in the Doppler axis, however, shows high sidelobes and wide mainlobe resulting in limited Doppler resolution. The 3 dB mainlobe width is approximately a whole Doppler cell, i.e., it corresponds to Doppler resolution of 13750 KHz, which corresponds to a velocity resolution of 34.375 m/s. The velocity resolution, however, can be improved by increasing the CPI duration. We can infer also from Fig. 5.6 that gain of the target vehicle is less than the clutter vehicle. This is because the target vehicle is farther, as compared to the clutter vehicle, from the source vehicle. This example illustrates the limit of velocity resolution, which is highly dependent on the duration of a CPI. At the same time, it also illustrates the ultra-low resolution and sidelobes in the range dimension which allows us to achieve cm-level range accuracy.

Chapter 6

Conclusions

Commercially available vehicular radars are expensive and use proprietary waveforms. Alternative Gbps mmWave WLAN communication options are much cheaper and standardized, but have yet to enter the vehicular market. This thesis showed that we can achieve the performance of a commercial automotive LRR using a low-cost IEEE 802.11ad system with minimal modifications, paving the way for a high data rate vehicular communication market. This thesis developed a mathematical framework for IEEE 802.11ad V2V-radar that bridges the gap between automotive LRR and mmWave WLAN systems. Our model exploits the preamble structure (GCP and repeated GCS) in IEEE 802.11ad and leveraged standard WLAN receiver techniques to propose pulse-Doppler-based automotive radar algorithms. Different single- and multi-frame techniques for the estimation of radar parameters were explored and their performance was evaluated both analytically and by simulations. The target vehicle is detected accurately at significantly lower constant false alarm rate for SCNR above 0 dB. The proposed range estimation algorithms using the STF and the CEF peak detection technique achieved better resolution and accuracy than the minimum requirement of LRR specifications (0.5 m range resolution and 0.1 m range accuracy). The velocity estimation tech-

nique performed well at high SCNR using single frame processing, and met the desired accuracy and resolution of 0.1 m/s and 0.6 m/s at low SCNR using multiple frame processing. Although the performance of velocity estimation depends on the duration of a CPI, which dictates the number and duration of training samples for integration, it achieved high accuracy and resolution for a CPI of 0.25 ms with Gbps data rate. These results indicate that IEEE 802.11ad V2V-radar is a promising option for next-generation automotive applications.

Appendices

Appendix A

Cramer Rao Lower Bound (CRLB) for Velocity Estimation

Consider the received training sequence $\mathbf{p} \in \mathbb{C}^{PM\times 1}$ in (4.12), which can also be expressed using

$$p[k_i + mK] = r[k_i + mK] + z_m[k_i] \quad 0 \le i \le P-1,\ 0 \le m \le M-1 \quad \text{(A.1)}$$

where $k_i = iK_{\mathrm{D}}$ is the sample number corresponding to the training symbol in a frame, K_{D} is the distance between two training sequences chosen in a frame, $r[k_i + mK] = \sqrt{\mathcal{E}_{\mathrm{s}} G_0} h_0(\mathbf{\Lambda}_0) x[k_i - \ell_0] e^{j\omega_0(k_i+mK)}$, $\omega_0 = 2\pi\nu_0 T_{\mathrm{D}}$, T_{D} is the duration between the two consecutive training symbols used for correlation, and K is the total number of samples in a frame. The clutter-plus-noise term $z_m[k_i]$ is assumed to be distributed as $\mathcal{CN}(0, \sigma^2_{\mathrm{cn}})$.

To calculate the CRLB, we will estimate $\Theta = [\sqrt{\mathcal{E}_{\mathrm{rad}}},\ \omega_0, \angle h_0(\mathbf{\Lambda}_0)]$ using Fisher information matrix $\mathbf{I}_\Theta$, where

$$\mathbf{I}_\Theta[x, y] = \frac{2}{\sigma^2_{\mathrm{cn}}} \Re \left\{ \sum_{n=0}^{PM-1} \left[\frac{\partial r[n]}{\partial \Theta_x}\right] \left[\frac{\partial r[n]}{\partial \Theta_y}\right]^* \right\} \quad \text{(A.2)}$$

where $n = k_i + mK$. After simplifying, we obtain the complete matrix as [55],

$$\mathbf{I}_\Theta = 2\frac{|\mathcal{E}_{\mathrm{rad}}|^2}{\sigma^2_{\mathrm{cn}}} \begin{bmatrix} PM/|\mathcal{E}_{\mathrm{rad}}|^2 & 0 & 0 \\ 0 & 4\pi^2 \sum_{i=0}^{PM-1} n^2 & 2\pi \sum_{i=0}^{PM-1} n \\ 0 & 2\pi \sum_{i=0}^{PM-1} n & PM \end{bmatrix}. \quad \text{(A.3)}$$

The CRLB corresponding to $\omega_0 = 2\pi\nu_0 T_{\mathrm{D}}$ estimation is the second diagonal element of $\mathbf{I}_{\Theta}^{-1}$ given by [60, 61]

$$\sigma_{\hat{\omega}}^2 \geq \frac{PM\frac{\mathcal{E}_{\mathrm{rad}}}{\sigma_{\mathrm{cn}}^2}+1}{2PM\left(\frac{\mathcal{E}_{\mathrm{rad}}}{\sigma_{\mathrm{cn}}^2}\right)^2}\left[\sum_{n=0}^{PM-1} n^2 - \frac{1}{PM}\left(\sum_{n=0}^{PM-1} n\right)^2\right]^{-1}. \tag{A.4}$$

For $\frac{\mathcal{E}_{\mathrm{rad}}}{\sigma_{cn}^2} \gg (1/P)$ and for consecutive samples in a single frame, i.e., $k_i = iK_{\mathrm{D}}$, $T_{\mathrm{D}} = K_{\mathrm{D}}T_{\mathrm{s}}$ and $m = 1$, CRLB can be further simplified into

$$\sigma_{\hat{\omega}}^2 \geq \frac{6}{(\mathcal{E}_{\mathrm{rad}}/\sigma_{\mathrm{cn}}^2)P(P^2-1)} \approx \frac{6}{P^3(\mathcal{E}_{\mathrm{rad}}/\sigma_{\mathrm{cn}}^2)}. \tag{A.5}$$

The CRLB for estimation of the Doppler shift ν_0 in Hz, can be expressed as

$$\sigma_{\hat{\nu}}^2 \geq \frac{6}{(2\pi)^2 T_{\mathrm{D}}^2(\mathcal{E}_{\mathrm{rad}}/\sigma_{\mathrm{cn}}^2)P(P^2-1)} \approx \frac{6}{(2\pi)^2 P^3 T_{\mathrm{D}}^2(\mathcal{E}_{\mathrm{rad}}/\sigma_{\mathrm{cn}}^2)}. \tag{A.6}$$

The best achievable precision of the Doppler shift estimate is provided by taking the square root of its CRLB, i.e.,

$$\sigma_{\hat{\nu}} \geq \frac{\sqrt{3}\Delta\nu}{\pi\sqrt{2P(\mathcal{E}_{\mathrm{rad}}/\sigma_{\mathrm{cn}}^2)}}, \tag{A.7}$$

where $\Delta\nu = 1/(PT_{\mathrm{D}})$ is the spectral resolution. Since the velocity is related to the Doppler shift by (3.6), the accuracy in velocity can be expressed as

$$\sigma_{\hat{v}} = \frac{\lambda}{2}\sigma_{\hat{\nu}} \tag{A.8}$$

and the velocity resolution is

$$\Delta v = \frac{\lambda}{2PT_{\mathrm{D}}}. \tag{A.9}$$

In case when $\mathbf{p}$ is composed of non-consecutive training sequence, i.e., $n = i + mK$, $T_{\mathrm{D}} = KT_{\mathrm{s}}$, then for large number of frames, i.e., large M, we can simplify (A.4) as

$$\sigma_{\hat{\nu}}^2 \geq \frac{6}{4\pi^2(MP^3 + M^3PK^2)T_{\mathrm{s}}^2(\mathcal{E}_{\mathrm{rad}}/\sigma_{\mathrm{cn}}^2)} \tag{A.10}$$

and the velocity resolution is

$$\Delta v = \frac{\lambda}{2MT_{\mathrm{D}}}. \tag{A.11}$$

Bibliography

[1] S. Saponara, M. Greco, E. Ragonese, G. Palmisano, and B. Neri, *Highly Integrated Low Power Radars*. Artech House, 2014.

[2] J. Wenger, "Automotive radar-status and perspectives," in *Proceedings of the IEEE Compound Semiconductor Integrated Circuit Symposium*, October 2005, pp. 21–25.

[3] H. H. Meinel and J. Dickmann, "Automotive radar: From its origins to future directions," *Microwave Journal*, vol. 56, no. 9, pp. 24–40, 2013.

[4] P. Papadimitratos, A. La Fortelle, K. Evenssen, R. Brignolo, and S. Cosenza, "Vehicular communication systems: Enabling technologies, applications, and future outlook on intelligent transportation," *IEEE Communications Magazine*, vol. 47, no. 11, pp. 84–95, 2009.

[5] J. B. Kenney, "Dedicated short-range communications (DSRC) standards in the United States," in *Proceedings of the IEEE*, vol. 99, no. 7, 2011, pp. 1162–1182.

[6] J. Choi, N. Gonzalez-Prelcic, R. Daniels, C. R. Bhat, and R. W. Heath Jr, "Millimeter wave vehicular communication to support massive automotive sensing," *arXiv preprint arXiv:1602.06456*, 2016.

[7] L. Han and K. Wu, "Joint wireless communication and radar sensing systems–state of the art and future prospects," *IET Microwaves, Antennas & Propagation*, vol. 7, no. 11, pp. 876–885, 2013.

[8] C. Sturm and W. Wiesbeck, "Waveform design and signal processing aspects for fusion of wireless communications and radar sensing," *Proceedings of the IEEE*, vol. 99, no. 7, pp. 1236–1259, 2011.

[9] G. N. Saddik, R. S. Singh, and E. R. Brown, "Ultra-wideband multifunctional communications/radar system," *IEEE Transactions on Microwave Theory and Techniques*, vol. 55, no. 7, pp. 1431–1437, 2007.

[10] C. R. Berger, B. Demissie, J. Heckenbach, P. Willett, and S. Zhou, "Signal processing for passive radar using OFDM waveforms," *IEEE Journal of Selected Topics in Signal Processing*, vol. 4, no. 1, pp. 226–238, 2010.

[11] L. Reichardt, C. Sturm, F. Grunhaupt, and T. Zwick, "Demonstrating the use of the IEEE 802.11p car-to-car communication standard for automotive radar," in *Proceedings of the 6th European Conference on Antennas and Propagation (EUCAP)*, 2012, pp. 1576–1580.

[12] J. Hasch, E. Topak, R. Schnabel, T. Zwick, R. Weigel, and C. Waldschmidt, "Millimeter-wave technology for automotive radar sensors in the 77 GHz frequency band," *IEEE Transactions on Microwave Theory and Techniques*, vol. 60, no. 3, pp. 845–860, 2012.

[13] H. Zhang, L. Li, and K. Wu, "24 GHz software-defined radar system for automotive applications," in *Proceedings of the 10th European Conference on Wireless Technology*, October 2007, pp. 138–141.

[14] L. Han and K. Wu, "Radar and radio data fusion platform for future intelligent transportation system," in *Proceedings of the 7th European Radar Conference (EuRAD)*, September 2010, pp. 65–68.

[15] P. Kumari, N. Gonzalez-Prelcic, and R. W. Heath Jr, "Investigating the IEEE 802.11ad Standard for Millimeter Wave Automotive Radar," in *Proceedings of the 82nd IEEE Vehicular Technology Conference*, September 2015, pp. 3587–3591.

[16] M. G. Parker, K. G. Paterson, and C. Tellambura, "Golay complementary sequences," *Encyclopedia of Telecommunications*, 2003.

[17] "Wireless LAN Medium Access Control (MAC) and Physical Layer (PHY) Specifications. Amendment 3: Enhancements for Very High Throughput in the 60 GHz Band," *IEEE Std. 802.11ad*, 2012.

[18] R. Turyn, "Ambiguity functions of complementary sequences (corresp.)," *IEEE Transactions on Information Theory*, vol. 9, no. 1, pp. 46–47, 1963.

[19] A. Pezeshki, R. Calderbank, S. D. Howard, and W. Moran, "Doppler resilient Golay complementary pairs for radar," in *IEEE/SP 14th Workshop on Statistical Signal Processing (SSP'07)*, 2007, pp. 483–487.

[20] A. Pezeshki, A. R. Calderbank, W. Moran, and S. D. Howard, "Doppler resilient Golay complementary waveforms," *IEEE Transactions on Information Theory*, vol. 54, no. 9, pp. 4254–4266, 2008.

[21] C. Karnfelt, A. Péden, A. Bazzi, G. Shhadé, M. Abbas, T. Chonavel, and F. Bodereau, "77 GHz ACC radar simulation platform," *Proccedings of the 2009 International Transport System Technology Symposium*, pp. 20–22, 2009.

[22] N. Levanon and E. Mozeson, *Radar signals*. John Wiley & Sons, 2004.

[23] A. Sabharwal, P. Schniter, D. Guo, D. Bliss, S. Rangarajan, and R. Wichman, "In-band full-duplex wireless: challenges and opportunities," *IEEE Journal on Selected Areas in Communications*, vol. 32, no. 9, pp. 1637–1652, September 2013.

[24] Wil6200: Second Generation WiGig and 802.11ad Multi-Gigabit Wireless Chipset. [Online]. Available: http://wilocity.com/resources/Wil6200-Brief.pdf

[25] W. Roh, J.-Y. Seol, J. Park, B. Lee, J. Lee, Y. Kim, J. Cho, K. Cheun, and F. Aryanfar, "Millimeter-wave beamforming as an enabling technology for 5G cellular communications: theoretical feasibility and prototype results," *IEEE Communications Magazine*, vol. 52, no. 2, pp. 106–113, 2014.

[26] V. Va, J. Choi, and R. W. Heath Jr, "The impact of beamwidth on temporal channel variation in vehicular channels and its implications," *Submitted to IEEE Transactions on Vehicular Technology*, 2015.

[27] W. David, "FMCW MMW radar for automotive longitudinal control," *California Partners for Advanced Transit and Highways (PATH)*, 1997.

[28] S. K. Saha, V. V. Vira, A. Garg, and D. Koutsonikolas, "60 GHz Multi-Gigabit Indoor WLANs: Dream or Reality?" *arXiv preprint arXiv:1509.04274*, 2015.

[29] H. Rohling and R. Mende, "OS CFAR performance in a 77 GHz radar sensor for car application," in *Proceedings of 1996 CIE International Conference of Radar*, 1996, pp. 109–114.

[30] A. Bazzi, C. Kärnfelt, A. Peden, T. Chonavel, P. Galaup, and F. Bodereau, "Estimation techniques and simulation platforms for 77 GHz FMCW ACC radars," *The European Physical Journal Applied Physics*, vol. 57, no. 01, p. 11001, 2012.

[31] M. A. Richards, "Signal models," in *Fundamentals of radar signal processing*. Tata McGraw-Hill Education, 2005, ch. 3, pp. 41–106.

[32] M. R. Akdeniz, Y. Liu, M. K. Samimi, S. Sun, S. Rangan, T. S. Rappaport, and E. Erkip, "Millimeter wave channel modeling and cellular capacity evaluation," *IEEE Journal on Selected Areas in Communications*, vol. 32, no. 6, pp. 1164–1179, 2014.

[33] A. F. Molisch, F. Tufvesson, J. Karedal, and C. F. Mecklenbräuker, "A survey on vehicle-to-vehicle propagation channels," *IEEE Wireless Communications*, vol. 16, no. 6, pp. 12–22, 2009.

[34] W. Menzel and A. Moebius, "Antenna concepts for millimeter-wave automotive radar sensors," *Proceedings of the IEEE*, vol. 100, no. 7, pp. 2372–2379, 2012.

[35] C. A. Balanis, *Antenna theory: analysis and design*. John Wiley & Sons, 2016.

[36] J. Li and P. Stoica, "MIMO radar with colocated antennas," *IEEE Signal Processing Magazine*, vol. 24, no. 5, pp. 106–114, 2007.

[37] A. Sayeed and T. Sivanadyan, "Wireless communication and sensing in multipath environments using multiantenna transceivers," *Handbook on Array Processing and Sensor Networks*, 2010.

[38] M. A. Richards, "Signal models," in *Fundamentals of radar signal processing*. Tata McGraw-Hill Education, 2005, ch. 2, pp. 41–106.

[39] O. Bar-Ilan and Y. C. Eldar, "Sub-Nyquist radar via Doppler focusing," *IEEE Transactions on Signal Processing*, vol. 62, no. 7, pp. 1796–1811, 2014.

[40] Q. He, N. H. Lehmann, R. S. Blum, and A. M. Haimovich, "MIMO radar moving target detection in homogeneous clutter," *IEEE Transactions on Aerospace and Electronic System*, vol. 46, no. 3, pp. 1290–1301, 2010.

[41] W. U. Bajwa, J. Haupt, A. M. Sayeed, and R. Nowak, "Compressed channel sensing: A new approach to estimating sparse multipath channels," *Proceedings of the IEEE*, vol. 98, no. 6, pp. 1058–1076, 2010.

[42] S. Geng, J. Kivinen, X. Zhao, and P. Vainikainen, "Millimeter-wave propagation channel characterization for short-range wireless communications," *IEEE Transactions on Vehicular Technology*, vol. 58, no. 1, pp. 3–13, 2009.

[43] P. A. Bello, "Characterization of randomly time-variant linear channels," *IEEE transactions on Communications Systems*, vol. 11, no. 4, pp. 360–393, 1963.

[44] M. A. Richards, "Detection fundamentals," in *Fundamentals of radar signal processing*. Tata McGraw-Hill Education, 2005, ch. 6, pp. 295–368.

[45] A. Sayeed and N. Behdad, "Continuous aperture phased MIMO: Basic theory and applications," in *48th Annual Allerton Conference on Communication, Control, and Computing (Allerton)*, 2010, pp. 1196–1203.

[46] J. Brady and A. Sayeed, "Beamspace mu-mimo for high-density gigabit small cell access at millimeter-wave frequencies," in *15th International Workshop on Signal Processing Advances in Wireless Communications (SPAWC)*, 2014, pp. 80–84.

[47] A. Chiriyath and D. Bliss, "Effect of clutter on joint radar-communications

system performance inner bounds," in *49th Asilomar Conference on Signals, Systems and Computers*, 2015, pp. 1379–1383.

[48] G. M. Brooker, "Mutual interference of millimeter-wave radar systems," *IEEE Transactions on Electromagnetic Compatibility*, vol. 49, no. 1, pp. 170–181, 2007.

[49] N. A. Estep, D. L. Sounas, J. Soric, and A. Alù, "Magnetic-free non-reciprocity and isolation based on parametrically modulated coupled-resonator loops," *Nature Physics*, vol. 10, no. 12, pp. 923–927, 2014.

[50] B. Paul and D. W. Bliss, "Extending joint radar-communications bounds for fmcw radar with doppler estimation," in *IEEE Radar Conference (RadarCon)*, 2015, pp. 0089–0094.

[51] M. I. Skolnik, *Radar Systems*. McGraw-Hill, NY, 2001.

[52] W.-C. Liu, T.-C. Wei, Y.-S. Huang, C.-D. Chan, and S.-J. Jou, "All-Digital Synchronization for SC/OFDM Mode of IEEE 802.15. 3c and IEEE 802.11ad," *IEEE Transactions on Circuits and Systems I: Regular Papers*, vol. 62, no. 2, Feb. 2015.

[53] G. Bo, Z. Changming, J. Depeng, and Z. Lieguang, "Compressed SNR-and-channel estimation for beam tracking in 60-GHz WLAN," *Communications, China*, vol. 12, no. 6, pp. 46–58, 2015.

[54] P. H. Moose, "A technique for orthogonal frequency division multiplexing frequency offset correction," vol. 42, no. 10, 1994, pp. 2908–2914.

[55] M. A. Richards, "Measurements and tracking," in *Fundamentals of radar signal processing*. Tata McGraw-Hill Education, 2005, ch. 7, pp. 369–440.

[56] A. R. Chiriyath, B. Paul, G. M. Jacyna, and D. W. Bliss, "Inner bounds on performance of radar and communications co-existence," *IEEE Transactions on Signal Processing*, vol. 64, no. 2, pp. 464–474, 2016.

[57] R. Bosch, "LRR3 3rd Generation Long-Range Radar Sensor," *Robert Bosch GmbH, Germany*, 2009.

[58] Part 15 Rules for Unlicensed Operation in the 57-64 GHz Band. [Online]. Available: http://www.fcc.gov/document/part-15-rules-unlicensed-operation-57-64-ghz-band/

[59] J. B. Billingsley, *Low-angle radar land clutter: measurements and empirical models*. William Andrew Publishing, 2002.

[60] V. M. Baronkin, Y. V. Zakharov, and T. C. Tozer, "Cramer-Rao lower bound for frequency estimation in multipath rayleigh fading channels," in *Proceedings of International Conference on Acoustics, Speech, and Signal Processing (ICASSP'01)*, vol. 4, 2001, pp. 2557–2560.

[61] J. Gansman, J. Krogmeier, and M. Fitz, "Single frequency estimation with non-uniform sampling," in *Proceedings of 13th Asilomar Conference on Signals, Systems and Computers*, vol. 1, 1996, pp. 399–403.

Vita

Preeti Kumari is a graduate student at the University of Texas at Austin. Prior to being a graduate student, she was a Scientist in the Indian Space Research Organisation (ISRO). She completed her Bachelor of Technology in Electronics and Telecommunication Engineering from Shri Guru Gobind Singhji Institute of Engineering and Technology (SGGSIE&T), Nanded, India. Her research interests include signal processing, radar and wireless communication.

Permanent address: preeti_kumari@utexas.edu

This thesis was typeset with LaTeX[†] by the author.

[†]LaTeX is a document preparation system developed by Leslie Lamport as a special version of Donald Knuth's TeX Program.